Title	Bridging theory and observations: insights into star formation efficiency and dust attenuation in z > 5 Galaxies
Author(s)	Toyouchi, Daisuke; Yajima, Hidenobu; Ferrara, Andrea et al.
Citation	Monthly Notices of the Royal Astronomical Society. 2025, 541(4), p. 3606-3626
Version Type	VoR
URL	https://hdl.handle.net/11094/102940
rights	This article is licensed under a Creative Commons Attribution 4.0 International License.
Note	

Bridging theory and observations: insights into star formation efficiency and dust attenuation in $z > 5$ Galaxies

Daisuke Toyouchi [ORCID],[1]★ Hidenobu Yajima [ORCID],[2] Andrea Ferrara[3] and Kentaro Nagamine [ORCID][1,4,5,6,7]

[1]*Theoretical Astrophysics, Department of Earth & Space Science, Graduate School of Science, Osaka University, 1-1 Machikaneyama, Toyonaka, Osaka, 560-0043, Japan*
[2]*Center for Computational Sciences, University of Tsukuba, 1-1-1 Tennodai, Tsukuba, Ibaraki 305-8577, Japan*
[3]*Scuola Normale Superiore, Piazza dei Cavalieri 7, I-50126 Pisa, Italy*
[4]*Theoretical Joint Research, Forefront Research Center, Graduate School of Science, The University of Osaka, Toyonaka, Osaka 560-0043, Japan*
[5]*Kavli IPMU (WPI), UTIAS, The University of Tokyo, Kashiwa, Chiba 277-8583, Japan*
[6]*Department of Physics & Astronomy, University of Nevada, Las Vegas, 4505 S. Maryland Pkwy, Las Vegas, NV 89154-4002, USA*
[7]*Nevada Center for Astrophysics, University of Nevada, Las Vegas, 4505 S. Maryland Pkwy, Las Vegas, NV 89154-4002, USA*

ABSTRACT

We investigate early galaxy evolution by modeling self-consistently their radially resolved evolution of gas, stars, heavy elements, and dust content. Our model successfully reproduces various observed properties of *JWST*-identified galaxies at $z > 5$, including sizes, stellar masses, star formation rates (SFR), metallicities, and dust-to-stellar mass ratios. We show that the star formation efficiency (SFE), $f_* \equiv \mathrm{SFR}/(f_\mathrm{b}\dot{M}_\mathrm{h})$, is regulated by the global equilibrium between cosmological gas inflows, star formation, and gas outflows. Our model predicts $f_* \lesssim 20$ per cent for galaxies with halo masses of $M_\mathrm{h} \sim 10^{11-12}\,\mathrm{M}_\odot$ down to $z = 5$, allowing them to reach intrinsic ultraviolet (UV) magnitudes of $M_\mathrm{UV} \lesssim -22$ mag; when dust attenuation is ignored, the predicted UV luminosity function (LF) at $z \sim 12$ agrees well with observations. However, our model also suggests that these galaxies would be heavily obscured by dust, with high optical depths at 1500 Å of $\tau_{1500} \gtrsim 10$, causing the dust-attenuated UV LF to fall significantly below the observed one. This discrepancy highlights the need for mechanisms that mitigate strong dust attenuation, such as dust evacuation from star-forming regions and/or preferential production of large dust grains. Further exploration of these processes is essential for understanding the early stages of galaxy evolution.

Key words: galaxies: evolution – galaxies: high-redshift – galaxies: luminosity function, mass function – galaxies: star formation.

1 INTRODUCTION

The *James Webb Space Telescope* (*JWST*) has significantly advanced our understanding of galaxy formation and evolution in the early universe. Its unprecedented capabilities provide a unique opportunity to investigate the properties of $z > 10$ galaxies that emerged within the first few hundred million years.

A notable finding from *JWST* observations is a higher abundance of $z > 10$ galaxies than expected from theoretical models, particularly at the bright end of the ultraviolet (UV) luminosity functions (LFs) (e.g. Yung et al. 2019; Behroozi et al. 2020; Mason, Trenti & Treu 2023; Wilkins et al. 2023), which also exhibit a surprisingly gradual evolution across $z \sim 9$–15 (e.g. Finkelstein et al. 2023; Harikane et al. 2023, 2025; Pérez-González et al. 2023; Adams et al. 2024; Donnan et al. 2024; McLeod et al. 2024). This trend appears to extend to even higher redshifts, as several galaxy candidates have been photometrically identified beyond $z = 20$ (Castellano et al. 2025; Pérez-González et al. 2025).

The observed galaxy UV LFs provide key insights into redshift dependence on star formation efficiencies (SFEs). Some theoretical studies have proposed a highly efficient star formation mode in $z > 10$ galaxies, driven by their extremely high gas densities leading to gas consumption time-scales shorter than the lifetimes of massive stars (Dekel et al. 2023; Li et al. 2024b). Indeed, Harikane et al. (2023) suggest that a constant SFE observed in $z \sim 2$–7 galaxies (Harikane et al. 2022) is insufficient to explain cosmic star formation rates at $z > 10$, implying an increase in SFEs toward higher redshifts. Conversely, Donnan et al. (2025) demonstrate with a simple model calculation that the observed UV LFs at $z > 10$ can be reproduced assuming an empirical stellar-to-halo mass relation derived at $z \simeq 0$, suggesting no significant evolution in SFEs across cosmic time. This raises the key question: what mechanisms govern SFEs within galaxies, and whether an increase of SFEs with redshift is truly necessary.

An alternative explanation for the bright-end UV LFs at high redshift is a top-heavy initial mass function (IMF), which would enhance the UV emissivity per unit star formation rate (SFR; e.g. Inayoshi et al. 2022; Wang et al. 2023a; Hutter et al. 2024; Trinca et al. 2024). For an IMF to be top-heavy, gas clouds in galaxies must have sufficiently low metallicities ($Z < 10^{-3}\,Z_\odot$) to suppress gas fragmentation due to metal cooling (e.g. Chon et al. 2024). However, recent *JWST* observations suggest that UV-bright galaxies at $z > 10$ already exhibit metallicities of $\gtrsim 0.1\,Z_\odot$ (Bunker et al. 2023; Castellano et al. 2024; D'Eugenio et al. 2024; Carniani et al.

★ E-mail: d.toyouchi@gmail.com

2024a, b), implying that their IMFs might have already settled onto a standard Salpeter-like distribution. Indeed, Cueto et al. (2024) argue that variations in the IMF due to metallicity alone are unable to explain the observed UV LF.

If these $z > 10$ galaxies are so metal-enriched, they are also likely to be dust-rich. For instance, assuming that the dust-to-gas mass ratio scales with metallicity, the dust mass in these galaxies could have already reached $\sim 10^5$ M$_\odot$. Moreover, given the compact sizes of $z > 10$ galaxies ($R_{\rm eff} \lesssim 200$ pc), they could become highly optically thick to UV radiation due to dust attenuation, with optical depths at 1500 Å of $\tau_{1500} \gtrsim 10$ and V-band extinction of $A_V \gtrsim 4$. This expectation, however, contradicts extremely blue UV slopes of these galaxies, suggesting minimal attenuation ($\beta < -2.2$; e.g. Topping et al. 2022; Cullen et al. 2024; Morales et al. 2024; Topping et al. 2024). To resolve this discrepancy, the attenuation-free model has been proposed, where radiation-driven outflows displace dust onto larger ($\sim$kpc) scales, thereby reducing the dust optical depth by several orders of magnitude (e.g. Ferrara, Pallottini & Dayal 2023; Fiore et al. 2023; Ziparo et al. 2023). Nevertheless, the attenuation-free scenario requires further investigation through a comprehensive analysis of UV-bright galaxies at $z > 10$, taking into account not only dust mass, but also galaxy size, metallicity, and their consistency with observed UV luminosities and number densities.

In this paper, we present a new galaxy evolution model that self-consistently incorporates galaxy size evolution, chemical enrichment, and dust formation. Using this model, we aim to reproduce various characteristics of *JWST*-identified galaxies at $z > 5$ and provide insights into key processes such as gas inflows and outflows that govern galaxy evolution. Furthermore, we examine SFEs of galaxies as a function of host halo mass and redshift, and discuss the requirements for dust attenuation to maintain consistency with the observed UV LFs. Our findings provide crucial insights into the physical processes shaping the galaxy evolution and their observational signatures at $z > 5$.

This paper is structured as follows. In Section 2, we describe the numerical setup of our galaxy evolution model. In Section 3, we compare our model predictions with recent observations of $z > 5$ galaxies, focusing on galaxy size, stellar mass, SFRs, metallicity, and dust properties. In Section 4, we investigate the SFEs of our model galaxies and their redshift evolution. In Section 5.1, we discuss the UV LFs of high redshift galaxies and highlight the necessity of reducing dust attenuation within galaxies. Potential mechanisms responsible for reducing dust attenuation are further explored in Section 5.2. In Section 5.3, we present the cosmic star formation rate density (CSFRD) obtained from our model and examine a weak-feedback scenario proposed to explain the observed CSFRD at $z > 10$. Finally, we summarize our conclusion in Section 6. Additionally, the observed properties of galaxies at $z \gtrsim 10$, which are compared with our model predictions, are listed in Table A1. Throughout this paper, we use the Planck cosmological parameter sets: $\Omega_{\rm m} = 0.3111$, $\Omega_\Lambda = 0.6899$, $\Omega_{\rm b} = 0.0489$, and $h = 0.6766$, and $\sigma_8 = 0.8102$ (Planck Collaboration VI 2020).

2 GALAXY EVOLUTION MODEL

2.1 Basic equations

We calculate galaxy evolution from $z = 20$ to $z = 5$, corresponding to the cosmic age of 0.18 and 1.2 Gyr, respectively. We assume that galaxies already possess entirely rotation-supported discs ($v/\sigma \gtrsim 1$, e.g. Parlanti et al. 2023; de Graaff et al. 2024; Kohandel et al. 2024; Nelson et al. 2024; Xu et al. 2024), conducting one-dimensional

calculations that space the disc structure with a logarithmic radial grid covering a range from $R_{\rm min} = 1$ pc to $R_{\rm max} = 10^4$ pc with 50 cells. At each radius, we calculate the time evolution of surface mass densities of gas, stars, and heavy elements, denoted as $\Sigma_{\rm g}$, Σ_*, and $Z\Sigma_{\rm g}$, respectively. The basic equations solved in this paper are written as follows:

$$\frac{\partial \Sigma_{\rm g}}{\partial t} = -\dot{\Sigma}_{\rm sf} + \dot{\Sigma}_{\rm in} - \dot{\Sigma}_{\rm out} + \dot{\Sigma}_{\rm ret} , \qquad (1)$$

$$\frac{\partial \Sigma_*}{\partial t} = \dot{\Sigma}_{\rm sf} - \dot{\Sigma}_{\rm ret} , \qquad (2)$$

$$\frac{\partial (Z\Sigma_{\rm g})}{\partial t} = -Z\dot{\Sigma}_{\rm sf} + Z_{\rm in}\dot{\Sigma}_{\rm in} - Z\dot{\Sigma}_{\rm out} + \dot{\Sigma}_{Z,\rm ret} , \qquad (3)$$

where $\dot{\Sigma}_{\rm sf}$, $\dot{\Sigma}_{\rm in}$, and $\dot{\Sigma}_{\rm out}$ are the surface densities of star formation rates, gas inflow rates, and gas outflow rates, respectively, whose specific expressions are introduced in the next subsection (Section 2.2). We set the metallicity of inflowing gas as $Z_{\rm in} = 0$, considering metal-free gas inflows for simplicity. $\dot{\Sigma}_{\rm ret}$ and $\dot{\Sigma}_{Z,\rm ret}$ represent mass-return rates of gas and heavy elements via stellar evolution, which are described as follows:

$$\dot{\Sigma}_{\rm ret} = \int_{m(t=t_1)}^{m_{\rm max}} m_{\rm ret}(m, Z(t')) \dot{\Sigma}_{\rm sf}(t') \frac{\phi(m, Z(t'))}{\rm M_\odot} {\rm d}m , \qquad (4)$$

$$\dot{\Sigma}_{Z,\rm ret} = \int_{m(t=t_1)}^{m_{\rm max}} \left(m_{\rm II}(m, Z(t')) + Z(t')m_{\rm ret}(m, Z(t')) \right)$$
$$\times \dot{\Sigma}_{\rm sf}(t') \frac{\phi(m, Z(t'))}{\rm M_\odot} {\rm d}m , \qquad (5)$$

where m denotes the initial mass of progenitor stars in unit of M$_\odot$, ϕ is the mass-normalized IMF, given by $\int_{m_{\rm min}}^{m_{\rm max}} m\phi(m) {\rm d}m = 1$ M$_\odot$ ($m_{\rm min} = 0.04$ M$_\odot$ and $m_{\rm max} = 150$ M$_\odot$), $m_{\rm ret}$ is the return mass from a star, $m_{\rm II}$ is the mass of heavy elements synthesized and released by a type-II supernova, $t_1(m)$ is the main-sequence stellar lifetime, and we define $t' \equiv t - t_1(m)$. We model the stellar lifetime with the fitting formula proposed by Schaller et al. (1992):

$$\tau(m) = \frac{2.5 \times 10^3 + 6.7 \times 10^2 m^{2.5} + m^{4.5}}{3.3 \times 10^{-2} m^{1.5} + 3.5 \times 10^{-1} m^{4.5}} \text{ Myr} . \qquad (6)$$

We evaluate $m_{\rm ret}$ and $m_{\rm II}$ based on the metallicity-dependent table provided by Nomoto, Kobayashi & Tominaga (2013). Note here that we ignore the chemical enrichment from type Ia supernovae since it is expected to be inactive at $z > 5$ yet owing to the long delay time of ~ 0.5 Gyr (e.g. Matteucci & Greggio 1986; Matteucci & Recchi 2001; Maoz, Sharon & Gal-Yam 2010). Finally, we adopt a metallicity-dependent IMF derived from radiation hydrodynamics simulations by Chon et al. (2024), who investigated stellar cluster formation across varying gas metallicities. The IMF is approximated as follows:

$$\phi = \phi_0 m^{-\alpha} \left[1 - \exp\left(-\left(\frac{m}{m_0}\right)^c \right) \right] \exp\left(-\frac{m_{\rm min}}{m} - \frac{m}{m_{\rm max}} \right) , \quad (7)$$

$$\alpha = 2.3 + 0.33 \log\left(\frac{Z}{Z_\odot}\right) , \qquad (8)$$

$$\log(m_0) = 0.2 + 0.45 \log\left(\frac{Z}{Z_\odot}\right) , \qquad (9)$$

where we fix $c = 1.6$ and $Z_\odot = 0.02$ is the metal-to-gas mass ratio of the Sun. This formulation predicts a top-heavy IMF with $\alpha \sim 1$ for $Z = 10^{-4} Z_\odot$, which gradually turns into a Salpeter-like one with $\alpha = 2.3$ for $Z = Z_\odot$.

Finally, we acknowledge that equations (1) and (3) do not account for radial gas advection across the galactic disc. In Appendix B, we explore the potential effect of this process through a post-processing analysis of our model results and find that radial advection is likely

negligible at $z \gtrsim 7$, where the gas densities of galactic discs are primarily determined by high gas inflow rates driven by cosmological mass assembly (see Fig. B1). Nevertheless, the dynamical structure of such high redshift galaxies and the nature of angular momentum redistribution remain poorly constrained. In particular, some UV-bright galaxies identified at $z > 10$ are too compact to be explained without efficient angular momentum extraction, possibly driven by intense disc instabilities, as discussed in Section 3.2. While our model reproduces such compact galaxies by phenomenologically reducing the spatial extent of gas inflows (Section 2.2), a self-consistent treatment of radial advection would be an important extension for future model calculations.

2.2 Star formation, inflow, and outflow

equations(1–3) can be solved by specifying functional forms of $\dot{\Sigma}_{\rm sf}$, $\dot{\Sigma}_{\rm in}$, and $\dot{\Sigma}_{\rm out}$. We model $\dot{\Sigma}_{\rm sf}$ based on the Kennicutt–Schmidt (KS) law (Schmidt 1959; Kennicutt 1998):

$$\dot{\Sigma}_{\rm sf} = 2.5 \times 10^{-4} \, \mathcal{F}_{\rm b} \left(\frac{\Sigma_{\rm g}}{\rm M_\odot \, pc^{-2}} \right)^{1.4} \rm M_\odot \, Myr^{-1} \, pc^{-2} \,, \qquad (10)$$

where we introduce a boost factor $\mathcal{F}_{\rm b} \geq 1$ to represent the tension in $\dot{\Sigma}_{\rm sf}$ from the original KS law. Recent observations have reported $\mathcal{F}_{\rm b} \sim 5$–$10$ for $z > 5$ galaxies (e.g. Vallini et al. 2024). This enhancement in $\dot{\Sigma}_{\rm sf}$ would result from the relatively high surface gas densities in high-z galaxies, which allow star-forming gas clouds to survive from stellar feedback, such as UV photoionization by massive stars (e.g. Kim, Kim & Ostriker 2018; Fukushima & Yajima 2021) and energy injection by supernovae (e.g. Grudić et al. 2018, 2020). However, it remains highly uncertain whether an elevated star formation law is essential to explain various observed properties of high-z galaxies (Donnan et al. 2025). To account for this uncertainty, we explore a range of $\mathcal{F}_{\rm b} = 1$–10 in our model, adopting a fiducial value of $\mathcal{F}_{\rm b} = 1$ to provide a conservative assessment of SFEs.

Galactic gas inflows occur as a natural consequence of cosmological mass assembly. In this study, we model the mass growth of dark matter haloes with a fitting formula from Fakhouri, Ma & Boylan-Kolchin (2010), which represents the mean growth rate of haloes with mass $M_{\rm h}$:

$$\dot{M}_{\rm h} = 46.1 \, \rm M_\odot \, yr^{-1} \left(\frac{\it M_{\rm h}}{10^{12} \, \rm M_\odot} \right)^{1.1}$$
$$\times (1 + 1.11 \, z)\sqrt{\Omega_{\rm m}(1+z)^3 + \Omega_\Lambda} \,. \qquad (11)$$

The total gas inflow rate is then expressed as,

$$\dot{M}_{\rm in} = f_{\rm b} \epsilon_{\rm in} \dot{M}_{\rm h} \,, \qquad (12)$$

where the cosmic baryon fraction is $f_{\rm b} \equiv \Omega_{\rm b}/\Omega_{\rm m} \sim 0.157$. The coefficient $\epsilon_{\rm in}$ accounts for phenomenological suppression of gas inflows caused by virial shock heating at the halo's outskirts (e.g. Birnboim & Dekel 2003; Kereš et al. 2005; Dekel & Birnboim 2006). The values of $\epsilon_{\rm in}$ have been specifically investigated by cosmological hydrodynamic simulations (e.g. Ocvirk, Pichon & Teyssier 2008; van de Voort et al. 2011). Following the recent simulation results by Correa et al. (2018), we model this suppression factor as,

$$\epsilon_{\rm in} = (1 + M_{\rm h}/M_{\rm h,ch})^k \,, \qquad (13)$$

where we set $M_{\rm h,ch} = 10^{12} \, \rm M_\odot$ and $k = -1$ to reproduce the behavior of cold gas flows at $z \sim 5$ (see also Waterval, Cannarozzo & Macciò 2025). Throughout this paper, we assume that $\epsilon_{\rm in}$ is independent of redshifts, as Correa et al. (2018) find that the redshift evolution of $M_{\rm h,ch}$ and k is trivial for $4 \leq z \leq 6$, whereas the evolution at $z > 6$ remains uncertain. This prescription for $\epsilon_{\rm in}$ effectively suppresses

the formation of extremely massive and UV-bright galaxies (e.g. $M_* > 10^{12} \, \rm M_\odot$ and $M_{\rm UV} < -24$ mag).

We model the radial distribution of gas inflow rates with an exponential radial profile, $\dot{\Sigma}_{\rm in} \propto \exp(-R/h_R)$, normalized by $\dot{M}_{\rm in} = 2\pi \int \dot{\Sigma}_{\rm in} R \, {\rm d}R$. This assumption is motivated by the ubiquitous exponential stellar profiles observed in star-forming galaxies over a broad redshift range, $z \sim 0$–16 (e.g. Freeman 1970; MacArthur, Courteau & Holtzman 2003; Elmegreen et al. 2005; Shibuya et al. 2015; Martorano et al. 2023; Ono et al. 2025). Then, we describe the scale length of the exponential profile as,

$$h_{\rm R} \equiv f_{\rm s} \lambda_{\rm s} r_{\rm vir} \,, \qquad (14)$$

where $r_{\rm vir} \propto M_{\rm h}^{1/3}(1+z)^{-1}$ is the virial radius of the host halo, $\lambda_{\rm s}$ is the spin parameter of the dark-matter halo, and $f_{\rm s}$ represents the ratio of the angular momentum of inflowing gas to that of dark matter.

Cosmological N-body simulations by Bullock et al. (2001) show that the spin parameter follows a log-normal distribution with a median value of $\bar{\lambda}_{\rm s} = 0.035$ and a standard deviation of $\sigma_\lambda = 0.5$. This implies that over 70 per cent of haloes have spin parameters in the range of $0.02 \lesssim \lambda_{\rm s} \lesssim 0.06$. For simplicity, we adopt a constant value of $\lambda_{\rm s} = \bar{\lambda}_{\rm s}$ throughout this paper.

On the other hand, the value of $f_{\rm s}$ can significantly deviate from unity due to baryonic processes. Stellar feedback can deposit angular momentum into the inflowing gas (e.g. Bekki, Tsujimoto & Chiba 2009; Gibson et al. 2013), while tidal torques from galaxy mergers can extract angular momentum (e.g. Hernquist 1989; Hopkins & Quataert 2010). To account for these effects, we explore a range $f_{\rm s} = 0.1$–2 in our model, adopting a fiducial value as $f_{\rm s} = 0.5$ to represent moderate angular momentum extraction.

Additionally, we assume that outflow rates from each radius scale with the local star formation rates, expressed as $\dot{\Sigma}_{\rm out} = \eta \, \dot{\Sigma}_{\rm sf}$, whose mass loading factor η determines the outflow efficiency. In this paper, we model η with a double power law function, following the results of cosmological simulations by Muratov et al. (2015) as,

$$\eta = \eta_0 \left\{ \frac{1}{2} \left(\frac{M_{\rm h}}{M_{\rm h,0}} \right)^{-1.1} + \frac{1}{2} \left(\frac{M_{\rm h}}{M_{\rm h,0}} \right)^{-0.33} \right\} \,. \qquad (15)$$

The change in the power-law indices generally corresponds to the transition from energy-conserving to momentum-conserving outflows. Supposing that outflow velocities scale with the circular velocities as $V_{\rm w} \propto M_{\rm h}^{1/3}$, the index of -0.33 for massive haloes represents momentum-driven winds ($\eta \propto V_{\rm w}^{-1}$). Conversely, the index of -1.1 for low-mass haloes is similar to but slightly steeper than the expectation for energy-driven winds ($\eta \propto V_{\rm w}^{-2}$). According to Muratov et al. (2015), the transition occurs at $M_{\rm h} \sim 10^{10}$–$10^{11} \, \rm M_\odot$, so that we adopt $M_{\rm h,0} = 10^{11} \, \rm M_\odot$ throughout this study. On the other hand, we treat η_0, the normalization of η at $M_{\rm h,0}$, as a free parameter. Previous hydrodynamic simulations have reported large uncertainties in η_0, with values ranging from unity to a few tens (Muratov et al. 2015; Christensen et al. 2016, 2018; Pandya et al. 2021; Harada, Yajima & Abe 2023). Therefore, we explore a broad range of $\eta_0 = 1$-100 and adopt a fiducial value of $\eta_0 = 5$, representing an intermediate case.

2.3 Dust content

Our model incorporates the dust formation in galaxies by solving the following mass conservation equation,

$$\frac{\partial(D\Sigma_{\rm g})}{\partial t} = \dot{\Sigma}_{\rm d}^{\rm pro} - \dot{\Sigma}_{\rm d}^{\rm ast} - \dot{\Sigma}_{\rm d}^{\rm des} - \dot{\Sigma}_{\rm d}^{\rm eje} + \dot{\Sigma}_{\rm d}^{\rm gro} \,, \qquad (16)$$

where the dust-to-gas mass ratio is $D \leq Z$. The five terms on the

right-hand side represent the following physical processes[1]:

(i) *Dust production:* $\dot{\Sigma}_d^{pro} = y_d \gamma_{II}$ is the dust production rate by SN II, where y_d is the dust yield per SN II, and $\gamma_{II} \equiv \int_{m_{II,min}}^{m_{II,max}} \dot{\Sigma}_{sf}(t') \phi(m, Z(t'))/M_\odot dm$ ($m_{II,min} = 10$ M$_\odot$ and $m_{II,max} = 40$ M$_\odot$) is the SN II occurrence rate per unit area and time. Throughout this paper, we adopt $y_d = 0.1$ M$_\odot$, which is a few times lower than the standard value (e.g. Todini & Ferrara 2001; Bianchi & Schneider 2007), but is required to explain the low dust-to-stellar mass ratio of $\lesssim 10^{-4}$ observed in $z > 10$ galaxies (Ferrara et al. 2024; Ferrara 2024b). This reduced dust yield is expected because, compared with local galaxies, $z \gtrsim 5$ galaxies have denser ISM owing to their compactness, so newly created dust by SN II would be efficiently destroyed through intense SN reverse shocks (e.g. Nozawa, Kozasa & Habe 2006; Nozawa et al. 2007; Leśniewska & Michałowski 2019; Slavin et al. 2020). Our model does not include dust production by AGB stars for simplicity, as their contribution is negligible at $z > 10$ due to their long stellar lifetimes (e.g. $\tau \sim 1$ Gyr for $m = 2$ M$_\odot$). Even at $z < 10$, the inclusion of AGB dust production is unlikely to significantly affect our results, since dust mass growth at lower redshifts is primarily driven by metal accretion onto dust grains (see the fifth item below).

(ii) *Dust astration:* $\dot{\Sigma}_d^{ast} = D\dot{\Sigma}_{sf}$ is the dust astration rate, where we assume that gas and dust are perfectly mixed in star-forming regions.

(iii) *Dust destruction:* $\dot{\Sigma}_d^{des} = (1 - X_c)D\Sigma_g/\tau_{des}$ is the destruction rate of preexisting dust by SN shock, where X_c is the mass fraction of cold ISM, which can avoid dust destruction, and we assume $X_c = 0.5$, based on recent high-z galaxy simulations by Pallottini et al. (2019). The dust destruction time-scale is expressed as,

$$\tau_{des} = \frac{\Sigma_g}{\epsilon \gamma_{II} m_{swep}} ,\qquad(17)$$

where we adopt the dust destruction efficiency of $\epsilon = 0.03$ and the ISM mass swept by SN shock of $m_{swep} = 6.8 \times 10^3$ M$_\odot$ (McKee 1989; Lisenfeld & Ferrara 1998).

(iv) *Dust ejection:* $\dot{\Sigma}_d^{eje} = D\dot{\Sigma}_{out}$ is the dust ejection rate via galactic outflows, where we assume that outflows have the same dust-to-gas mass ratio as that in ISM since dust likely couples with gas strongly by Coulomb and viscous drag forces.

(v) *Dust growth:* $\dot{\Sigma}_d^{gro}$ is the dust growth rate via accretion of heavy elements in cold ISM, which is written as

$$\dot{\Sigma}_d^{gro} = \left(1 - \frac{D}{Z}\right) \frac{X_c D\Sigma_g}{\tau_{acc}} .\qquad(18)$$

The accretion time-scale inversely scales with gas metallicity as $\tau_{acc} = \tau_0 (Z/Z_\odot)^{-1}$, where the normalization time-scale τ_0 is usually set to be 1–100 Myr. In this study, we adopt $\tau_0 = 5$ Myr as the fiducial value to explain the dust-deficiency of $z > 10$ galaxies and the dust-richness of $z \sim 7$ galaxies simultaneously, as shown in Section 3.4.

2.4 Stellar UV radiation and FIR dust continuum

Based on our calculation results, we estimate the UV surface brightness I_{UV} at any radius as,

$$I_{UV} = \frac{1}{2} \epsilon_{UV} \dot{\Sigma}_{sf} c^2 ,\qquad(19)$$

---

[1] Our model description of those dust physics is based on the semi-analytic model DELPHI presented by Dayal et al. (2022), so we recommend readers refer to their paper for details.

where a factor of 1/2 accounts for radiation emitted from both surfaces of the galactic disc, and ϵ_{UV} is the UV radiative efficiency, which increases with top-heavier IMFs. To model ϵ_{UV}, we fit the metallicity-dependent IMFs of Chon et al. (2024), obtaining the following relation:

$$\log(\epsilon_{UV}) = \log(\epsilon_{UV,0}) + A \left\{ 1 + \exp\left(\frac{[O/H] - [O/H]_0}{\sigma_{[O/H]}}\right) \right\}^{-1} ,\qquad(20)$$

where $\log(\epsilon_{UV,0}) = -3.463$, $[O/H]_0 = -1.308$, $\sigma_{[O/H]} = 0.335$, and $A = 0.601$.

This formulation predicts a sharp decline in ϵ_{UV} above $[O/H] \sim -2$, leading to a transition in UV luminosities. Specifically, at a fixed SFR, galaxies with $[O/H] < -2$ appear about three times brighter in the UV band compared to those with $[O/H] > -2$. However, we note that the top-heavy IMF in such metal-poor galaxies enhances supernova feedback, which in turn reduces SFRs. Semi-analytic calculations by Cueto et al. (2024) demonstrated that, due to this counteracting effect, metallicity-dependent IMFs alone cannot fully explain the observed abundance of UV-bright galaxies at $z > 10$, a finding consistent with the recent cosmological galaxy formation simulations by Oku & Nagamine (2024). While our model does not take into account the metallicity dependence of stellar feedback, such as variations in the mass loading factor (η), self-consistent modeling of both ϵ_{UV} and η as functions of metallicity remains an important subject for future research.

A fraction of UV photons are absorbed by dust grains within the galactic disc, so that the observed UV luminosity is reduced from the intrinsic value. We account for the dust attenuation by calculating dust optical depth at 1500 Å at each radius as,

$$\tau_{1500} = \kappa_{1500} D\Sigma_g \sim 17.3 \left(\frac{\Sigma_g}{10^4 \text{ M}_\odot \text{ pc}^{-2}}\right)\left(\frac{D/D_{MW}}{0.01}\right) ,\qquad(21)$$

where $D_{MW} = 6.2 \times 10^{-3}$ is the dust-to-gas mass ratio in the Milky Way (MW) galaxy, and $\kappa_{1500} = 1.26 \times 10^5$ cm^{2}g^{-1} is the dust mass absorption coefficient appropriate for a MW-like extinction curve (Weingartner & Draine 2001). Assuming a slab-like geometry, the escape fraction of UV continuum at 1500 Å is written by

$$f_{esc} = \frac{1 - \exp(-\tau_{1500})}{\tau_{1500}} ,\qquad(22)$$

and the attenuated UV luminosity is derived by integrating the surface brightness over the disc,

$$L_{UV} = 4\pi \int_{R_{min}}^{R_{max}} f_{esc} I_{UV} R dR .\qquad(23)$$

This equation also describes the intrinsic UV luminosity for $f_{esc} = 1$.

Dust grains that absorb UV photons emit the gained energy as continuum radiation in the far infrared (FIR) band. The FIR flux of dust continuum reflects the intrinsic UV luminosity and the spatial distribution of dust in the galaxy. Here, we compute the FIR flux at a rest frame wavelength of 158 μm since high-z ALMA observations are often tuned to detect [C II] 158 μm line emission. By considering the energy conservation, we model the local dust temperature at any radius as follows (e.g. Dayal, Hirashita & Ferrara 2010; Hirashita et al. 2014; Ferrara et al. 2022):

$$T_d = \left(\frac{I_{abs}}{\Theta D\Sigma_g}\right)^{1/(4+\beta_d)} ,\qquad(24)$$

where

$$\Theta = \frac{8\pi}{c^2} \frac{\kappa_{158}}{\nu_{158}^{\beta_d}} \frac{k_B^{4+\beta_d}}{h_P^{3+\beta_d}} \zeta(4+\beta_d)\Gamma(4+\beta_d) , \qquad (25)$$

and $I_{abs} = (1 - f_{esc})I_{UV}$ is the stellar UV radiation absorbed by dust. Here, we suppose the MW-like dust model, whose mass absorption coefficient is approximated as $\kappa_\nu = \kappa_{158}(\nu/\nu_{158})^{\beta_d}$ with $\beta_d = 2.03$, $\kappa_{158} = 10.41$ cm^{2}g^{-1}, and $\nu_{158} = c/(158\ \mu$m$)$. ζ and Γ are the Zeta and Gamma functions, respectively, and other symbols have the usual meaning. Additionally, we account for dust heating by the cosmic microwave background (CMB) radiation, whose temperature is $T_{CMB}(z) = T_0(1+z)$ with $T_0 = 2.7255$ K, by correcting the dust temperature with the following formula presented by da Cunha et al. (2013),

$$T_d' = \left\{ T_d^{4+\beta_d} + T_0^{4+\beta_d}[(1+z)^{4+\beta_d} - 1] \right\}^{1/(4+\beta_d)} . \qquad (26)$$

Finally, the total flux at the rest frame 158 μm from a galaxy is evaluated as,

$$F_{158} = 4\pi \int_{R_{min}}^{R_{max}} I_{158} R dR , \qquad (27)$$

where

$$I_{158} = \frac{1}{2} g(z)\kappa_{158} D\Sigma_g [B_{158}(T_d') - B_{158}(T_{CMB})] , \qquad (28)$$

and B_λ is the black-body spectrum, and $g(z) = (1+z)/d_L^2$ with the luminosity distance to the source d_L.

Thus, our model calculates the UV luminosity and the FIR flux self-consistently. It is worth noting here that the FIR dust continuum radiation from $z > 10$ UV-bright galaxies has not been detected yet (e.g. Fudamoto et al. 2024; Schouws et al. 2024; Zavala et al. 2024; Carniani et al. 2024a), even though their observed half-light radii are so small that the optical depth can be extremely high, $\tau \gtrsim 10$ (e.g. Ziparo et al. 2023; Ferrara et al. 2024). This observational fact provides an important indication of the dust content and its spatial distribution in such $z > 10$ galaxies. In Section 3.4 and 5.1, we address this point in more detail based on our model calculation.

3 RESULTS

3.1 Overview of our calculations

We apply our model to 21 dark matter haloes, whose redshift evolution of M_h is calculated using equation (11) and summarized in Fig. 1. From the bottom to the top, we set the initial mass of ith halo as $M_{h,i} = M_{h,1} \times 10^{\delta_i}$ with $\delta_i = (i-1)/20 \times \log(M_{h,21}/M_{h,1})$, where $M_{h,1} = 5.8 \times 10^7$ M$_\odot$ and $M_{h,21} = 5.2 \times 10^9$ M$_\odot$ correspond to the initial masses of the 1st (lightest) and 21st (heaviest) haloes. This setup ensures that the 1st, 5th, 9th, 13th, 17th, and 21st haloes grow up to $M_h = 10^{10}$, 10^{11}, 10^{12}, 10^{13}, and 10^{14} M$_\odot$ at $z = 5$, respectively. By incorporating these diverse halo mass growth histories, we can examine the galaxy evolution as a function of redshift and their host halo masses.

In this work, we perform model calculations by varying four parameters, $\mathcal{F}_b$, f_s, η_0, and τ_0. The ranges and fiducial values adopted in this study are summarized in Table 1. Comparing our model results with observations under different parameter sets provides valuable insights into star formation, gas inflows, gas outflows, and dust growth.

The upper panel of Fig. 2 shows the mass evolution of different components for a halo with $M_h(z = 5) = 10^{12}$ M$_\odot$, calculated with
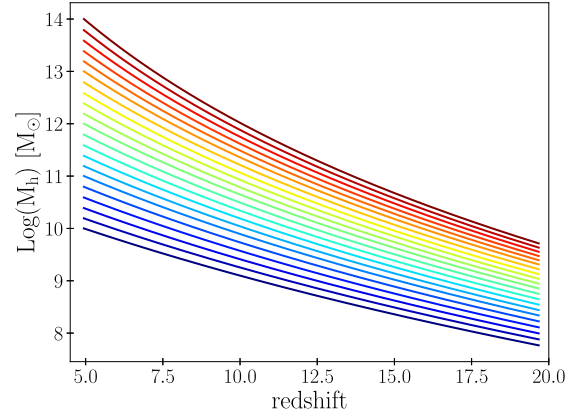
Figure 1. The redshift evolution of M_h for our 21 dark-matter haloes. The initial masses of the haloes are spaced on a uniform logarithmic grid, ranging from $M_h = 5.8 \times 10^7$ M$_\odot$ and 5.2×10^9 M$_\odot$ at $z = 20$. The halo masses evolve with equation (11), and the lightest and heaviest haloes grow to be $M_h = 10^{10}$ M$_\odot$ and 10^{14} M$_\odot$ at $z = 5$, respectively.

the fiducial parameters. The gas mass increases over time, scaling approximately with the halo mass growth, with a gas-to-dark matter mass ratio of $M_g/M_h \sim 0.01$. This value is about ten times lower than the cosmological baryon fraction ($f_b \sim 0.157$; Planck Collaboration VI 2020), reflecting high outflow rates of $\dot{M}_{out}$/SFR > 10. The stellar mass is initially much lower than but gradually catches up with the gas mass, resulting in a stellar mass fraction of $M_*/(M_g + M_*) \sim 0.3$ at $z = 5$. The mass evolution of heavy elements closely follows that of stellar mass, reflecting metal enrichment primarily driven by Type-II SNe. A notable feature is the rapid dust mass growth: while significantly lower than the metal mass at $z > 10$, the dust mass reaches approximately 70 per cent of the total metal mass by $z \sim 5$. This sharp increase in dust mass for $z < 8$ is primarily driven by metal accretion on dust grains, as discussed in more detail in Section 2.3.

The lower panel of Fig. 2 presents the radial profiles of surface mass densities for the fiducial galaxy at $z = 7$ and 12. At $z = 12$, the gas radial profile exhibits an exponential decay beyond $R \sim 200$ pc, marking the outer edge of the galactic disc; this cutoff radius increases to $R \sim 1$ kpc by $z = 7$. Despite the size growth, the gas mass density within the disc remains nearly constant at $\Sigma_g \sim 4 \times 10^3$ M$_\odot$ pc^{-2}. In contrast, the stellar mass density gradually increases, eventually surpassing the gas mass density by $z \sim 7$. At this redshift, the surface mass densities of metals reaches $Z\Sigma_g \sim 60$ M$_\odot$ pc^{-2}. The gas metallicity within the disc is $Z \sim 0.75$ Z$_\odot$ and nearly constant with radius. Such flat metallicity gradients are generally reported for star-forming galaxies observed at $z > 5$ (Arribas et al. 2024; Vallini et al. 2024; Venturi et al. 2024), while a more recent study by Li et al. (2023) identified steep negative gradients of ~ 0.4 dex kpc^{-1} even in $z \sim 7$ galaxies. It is worth noting that the weak radial variation of Z in our model may arise from the assumptions of a radially uniform mass loading factor and the absence of radial gas advection. To address this, we plan to modify our model by incorporating radially dependent outflows and redistribution of heavy elements, and we will discuss the resulting metallicity gradients in future work.

Finally, we note that the galactic disc has the surface dust mass densities of $D\Sigma_g \sim 20$ M$_\odot$ pc^{-2} at $z = 7$. The resulting dust-to-gas mass ratio within the disc of $D \sim 0.8$ D_{MW} corresponds to $\tau_{1500} \sim 800$ (see equation 21 and Fig. C1). This implies that the galaxy is heavily obscured in the UV band by dust. In the following

Table 1. The four free parameters in our model. We present, from left to right, their symbols, explored ranges, fiducial values, and descriptions.

Parameter	Range	Fiducial value	Description
$\mathcal{F}_b$	1–10	1	Boost factor that representing the enhancement in $\dot{\Sigma}_{sf}$ from the original KS law, defined by equation (10)
f_s	0.1–2	0.5	Ratio of angular momentum of inflowing gas to dark matter, defined by equation (14)
η_0	1–100	5	Outflow mass loading factor for $M_{h,0} = 10^{11}$ M$_\odot$, defined by equation (15)
τ_0	5–50 Myr	5 Myr	Time-scale of metal accretion onto dust at $Z = Z_\odot$, defined by equation (18)
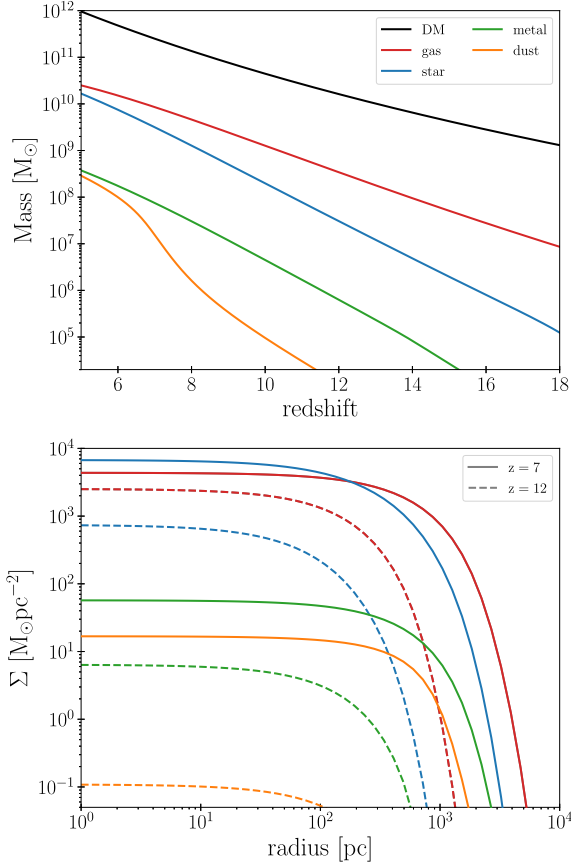
Figure 2. The mass evolution of different components for a single galaxy with $M_h(z = 5) = 10^{12}$ M$_\odot$, calculated with the fiducial parameters: $\mathcal{F}_b = 1$, $f_s = 0.5$, $\eta_0 = 5$, and $\tau_0 = 5$ Myr. The upper panel shows total masses of each component within the galaxy as a function of redshifts. The masses of dark matter, gas, star, metal, and dust are represented by black, red, blue, green, and orange curves, respectively. The lower panel shows the radial profiles of surface mass densities for each component in the galaxy. Solid and dashed curves correspond to the profiles at $z = 7$ and 12, respectively. The line colours are consistent with those used in the upper panel.

subsections, we further examine our results and discuss various observed properties of $z > 5$ galaxies.

3.2 Size evolution

First, we explore the redshift evolution of the UV half-light radius R_{eff}, which is defined as $L_{UV}(< R_{eff}) = 0.5\ L_{UV}(< R_{max})$ with equation (23). In this analysis, we evaluate R_{eff} using the intrinsic UV luminosity rather than the dust-attenuated one, motivated by the marginal dust extinction observed in $z > 5$ galaxies. Potential explanations for this minimal dust attenuation are discussed in Section 2.3.
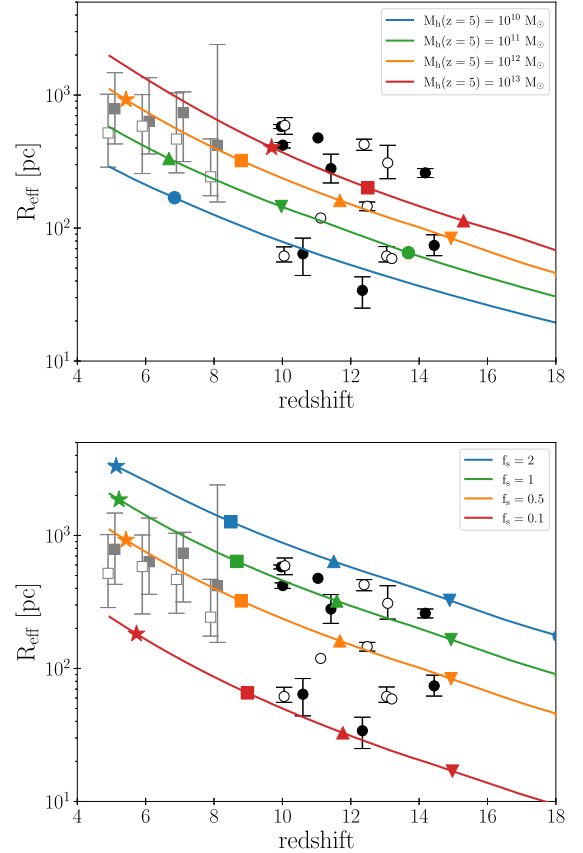
Figure 3. The redshift evolution of the UV half-light radii of galaxies predicted by our calculations. In the upper panel, the blue, green, orange, and red curves show predictions from our fiducial model for four haloes evolving to $M_h(z = 5) = 10^{10}$, 10^{11}, 10^{12}, and 10^{13} M$_\odot$, respectively. The lower panel presents results for a halo with $M_h(z = 5) = 10^{12}$ M$_\odot$, calculated with different gas angular momentum parameters of $f_s = 0.1$ (red), 0.5 (orange), 1 (green), and 2 (blue). All other parameters not specified here are set to their fiducial values. Coloured markers indicate the redshifts where the intrinsic UV absolute magnitude reaches $M_{UV} = -15$, -17, -19, -21, and -23 mag, represented by circles, inverted triangles, triangles, squares, and stars, respectively. For comparison, we also plot the half-light radii of Lyman-break galaxies with $M_{UV} \sim -19$ mag and -21 mag at $5 < z < 8$ with grey open and filled squares, respectively, where values are averaged over redshift bins (Shibuya, Ouchi & Harikane 2015). Additionally, the black open and filled circles correspond to galaxies with $M_{UV} > -20$ mag and < -20 mag, respectively, identified by *JWST* at $z \gtrsim 10$ (see Table A1 for references).

Fig. 3 compares R_{eff} predicted by our model with those derived from the HST and *JWST*. The upper and lower panels show how R_{eff} depends on M_h and f_s, respectively. We note that other parameters have a relatively minor impact on the size evolution. Our model demonstrates that more massive galaxies are spatially more extended, with their sizes gradually increasing toward lower redshifts, which is generally consistent with the observational trend. The evolution of

$R_{\rm eff}$ is attributed to our assumption that the spatial extent of galactic gas inflows scales with the virial radius, i.e. $h_{\rm R} \propto M_{\rm h}^{1/3}(1+z)^{-1}$. This indicates that the observed size evolution of $z > 5$ galaxies is a natural consequence of structure formation in the ΛCDM cosmology.

However, we note discrepancies between our model predictions and observed correlations between $M_{\rm UV}$ and $R_{\rm eff}$. Specifically, our calculations, fixing $f_{\rm s} = 0.5$ (upper panel), suggest that compact galaxies with $R_{\rm eff} < 100$ pc at $z \gtrsim 10$ are fainter than $M_{\rm UV} \sim -15$ mag. This prediction cannot explain the presence of very compact and bright galaxies, such as GN-z11 and GHZ2, which have $R_{\rm eff} \lesssim 100$ pc and $M_{\rm UV} < -20$ mag. Indeed, GN-z11 and GHZ2 may host active galactic nuclei (AGNs), thereby appearing as compact, UV-bright sources. However, the relative contributions of AGN and star formation to their UV luminosity remain highly uncertain (Castellano et al. 2024; Maiolino et al. 2024). If star formation dominates their UV luminosity, a possible solution to this discrepancy is a diversity in $f_{\rm s}$ among high-z galaxies.

As shown in the lower panel of Fig. 3, varying $f_{\rm s}$ from 0.1 to 2 for haloes with $M_{\rm h}(z = 5) = 10^{12}$ M$_\odot$ generally reproduces the wide range of $R_{\rm eff}$ observed for $z > 10$ galaxies. In particular, the case of $f_{\rm s} = 0.1$ produces GN-z11 and GHZ2-like galaxies around $z \sim 10$. This result suggests that such extremely compact galaxies in the early universe may have experienced efficient angular momentum extraction, potentially due to disc instabilities (Noguchi 1999; Immeli et al. 2004; Bournaud, Elmegreen & Elmegreen 2007) and galaxy mergers (Hernquist 1989; Barnes & Hernquist 1991, 1996; Hopkins & Quataert 2010).

3.3 Mass–XSFR–metallicity relation

Fig. 4 compares our calculated stellar mass–SFR–metallicity relation with corresponding observational data at different redshifts. From top to bottom, we show the results for varying $M_{\rm h}(z = 5)$, $\mathcal{F}_{\rm b}$, $f_{\rm s}$, and η_0. Overall, our model predictions are consistent with the observational data.

The left column of Fig. 4 presents the M_*–SFR relation, showing that our model naturally produces SFRs about 10–100 times higher than those for local galaxies with comparable stellar masses. We also find that SFRs increase with higher $M_{\rm h}$ and lower η_0, suggesting that the observed diversity in SFRs primarily reflects differences in halo mass growth histories and outflow strengths. In contrast, variations in $\mathcal{F}_{\rm b}$ and $f_{\rm s}$ have little impact on the evolutionary track in the M_*-SFR plane, even though higher $\mathcal{F}_{\rm b}$ and lower $f_{\rm s}$, which increases $\Sigma_{\rm g}$, likely enhance local star formation rates, $\dot{\Sigma}_{\rm sf}$. As we will demonstrate in Section 4, this independence of global SFRs from the local star formation law and galaxy sizes naturally arises from a self-regulated evolution: an elevated $\dot{\Sigma}_{\rm sf}$ rapidly depletes gas within galaxies, preventing a sustained increase in the global SFRs. Interestingly, this self-regulation process leads to a tight correlation between SFRs and $\dot{M}_{\rm h}$, suggesting that the enhanced SFRs in $z > 5$ galaxies primarily result from the large cosmological accretion rates in the early phase of galaxy evolution.

It is worth noting that our model predicts higher specific star formation rates SFR/M_* for lower-mass haloes and at higher redshifts. Consequently, galaxies with $M_{\rm h} \lesssim 10^{12}$ M$_\odot$ maintain SFR/$M_* \gtrsim 20$ Gyr^{-1} until $z \sim 10$. This satisfies the theoretical criterion for radiation pressure on dust grains to expel gas from galaxies (Fiore et al. 2023; Ferrara 2024a). Such radiation-driven dusty outflows may play a crucial role in explaining the observed number density of UV-bright galaxies at $z > 10$, as we discuss in Section 5.2.1.

The middle column of Fig. 4 shows the mass-metallicity relation, revealing a strong dependence of gas metallicity on η_0, while other parameters have relatively minor effects. Higher values of η_0 lead to lower metallicity due to the efficient evacuation of metals by outflows. Our models with $\eta_0 = 5$ and 20 closely match the median metallicity of the observational data, whereas models with $\eta_0 = 1$ and 100 correspond to the upper and lower edges of the observed metallicity distribution, respectively. This agreement implies that galaxies spectroscopically observed by *JWST* at $z > 5$ have a wide range of mass loading factors, varying by a few orders of magnitude, with an average value of $\eta_0 \sim 10$.

We also examine the fundamental metallicity relation, which $z \lesssim 3$ star-forming galaxies are known to follow. This relation is given by,

$$12 + \log({\rm O/H}) = 0.43\mu + 4.58 \, , \tag{29}$$

where $\mu = \log(M_*) - 0.66\log({\rm SFR})$ (e.g. Mannucci et al. 2010; Andrews & Martini 2013). Recent *JWST* observations of $z > 3$ galaxies indicate that their metallicities either follow the empirical law or are lower by a factor of a few (Bunker et al. 2023; Nakajima et al. 2023; Arrabal Haro et al. 2023b; Castellano et al. 2024; Curti et al. 2024; D'Eugenio et al. 2024; Sarkar et al. 2024; Carniani et al. 2024a). The right column of Fig. 4 compares these observational results with our model calculations, showing that the observed trend can be explained by supposing high mass loading factors ($\eta_0 \sim 5$–20). These values of η are generally consistent with, or somewhat higher than, those required by semi-analytical models to account for the extended [C II]-emitting haloes observed at $z = 4$–6 (e.g. $4 \gtrsim \eta \gtrsim 7$; Pizzati et al. 2020, 2023). Thus, we suggest that powerful outflows are prevalent in $z > 5$ galaxies, significantly impeding the progress of chemical enrichment.

3.4 Dust properties

Next, we explore the dust mass of galaxies ($M_{\rm d}$). Figs 5(a) and (b) show our calculation results with the fiducial case for the M_*–$M_{\rm d}$ relation and the redshift evolution of $M_{\rm d}/M_*$, respectively. Our calculations are generally in good agreement with observations, successfully reproducing the dust content of $z \sim 7$ galaxies and remaining consistent with the upper limits for the galaxies at $z > 10$ (GN-z11, GHZ2, and GS-z14-0). We suggest that dark matter haloes growing to $M_{\rm h}(z = 5) \gtrsim 10^{12}$ M$_\odot$ can represent dust-rich galaxies with $M_{\rm d} \gtrsim 10^7$ M$_\odot$ observed at $z \sim 7$.

A notable feature of our results is the rapid increase of $M_{\rm d}/M_*$ at $z < 10$, which is driven by dust growth via metal accretion. In our fiducial case ($\tau_0 = 5$ Myr), massive haloes with $M_{\rm h}(z = 5) \gtrsim 10^{12}$ M$_\odot$ achieve a short metal accretion time-scale $\tau_{\rm acc} \lesssim 50$ Myr at $z \lesssim 10$ since their metallicities have reached $Z \sim 0.1$ Z$_\odot$. As a result, this efficient metal accretion causes $M_{\rm d}/M_*$ to increase by an order of magnitude by $z = 5$. Such a rapid increase of $M_{\rm d}/M_*$ has also been reported by Burgarella et al. (2025), who estimated the dust content of 173 galaxies at $z = 4$–11 observed with *JWST*/NIRSpec, based on their inferred dust extinction.

To explore the impact of slower dust growth, we perform additional calculations assuming a longer time-scale ($\tau_0 = 50$ Myr), shown as dotted curves in Figs 5(a) and (b). In this case, $M_{\rm d}/M_*$ shows only marginal growth even after $z \sim 10$, highlighting the importance of efficient metal accretion for explaining the observed dust enrichment in $z \sim 7$ galaxies.

We also investigate the dust temperature of our model galaxies. With equation (24), we evaluate the dust temperature at any radii within the galaxies. For convenience, we average the dust
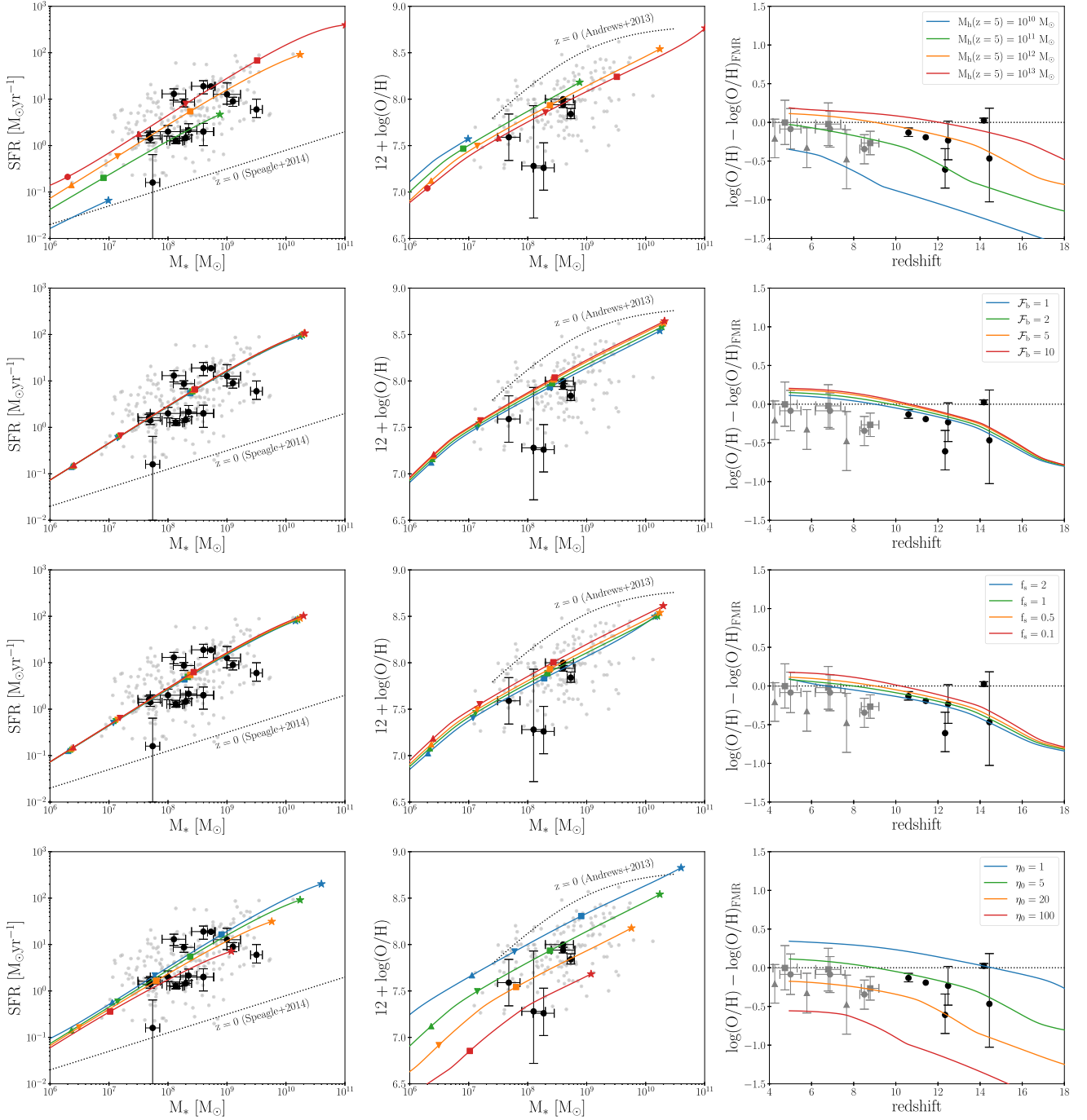
Figure 4. The relations between stellar mass, star formation rate, and metallicity obtained from our calculations. *Left column*: The M_*–SFR relation. *Middle column*: The M_*–$12 + \log(\mathrm{O/H})$ relations. *Right column*: The deviation in $12 + \log(\mathrm{O/H})$ from the fundamental metallicity relation derived by Andrews & Martini (2013) at any redshift. In the top row, the blue, green, orange, and red curves show predictions from our fiducial model for four haloes evolving to $M_\mathrm{h}(z = 5) = 10^{10}$, 10^{11}, 10^{12}, and 10^{13} $\mathrm{M}_\odot$, respectively. From the second to the fourth rows, the coloured curves in each panel represent results for a halo with $M_\mathrm{h}(z = 5) = 10^{12}$ $\mathrm{M}_\odot$, calculated with varying $\mathcal{F}_\mathrm{b}$, f_s, and η_0. Specific values for each parameter are noted in the top-right corner of the right panels, while other parameters not specified there are set to their fiducial values. In the left and middle column, coloured markers denote redshifts $z = 18$, 15, 13, 10, and 5, represented by circles, triangles, inverted triangles, squares, and stars, respectively. For comparison, we plot observational data for star-forming galaxies at $3 < z < 10$ (grey dots; Nakajima et al. 2023; Curti et al. 2024; Sarkar et al. 2024) and galaxies at $z > 10$ (black circles; see Table A1 for references). In the right column, grey circles, triangles, and squares represent redshift-binned values for $3 < z < 10$ galaxies from Nakajima et al. (2023), Curti et al. (2024), and Sarkar et al. (2024), respectively. Additionally, the M_*–SFR and M_*–$12 + \log(\mathrm{O/H})$ relations observed at $z = 0$ are shown as the dotted curves (Andrews & Martini 2013; Speagle et al. 2014).
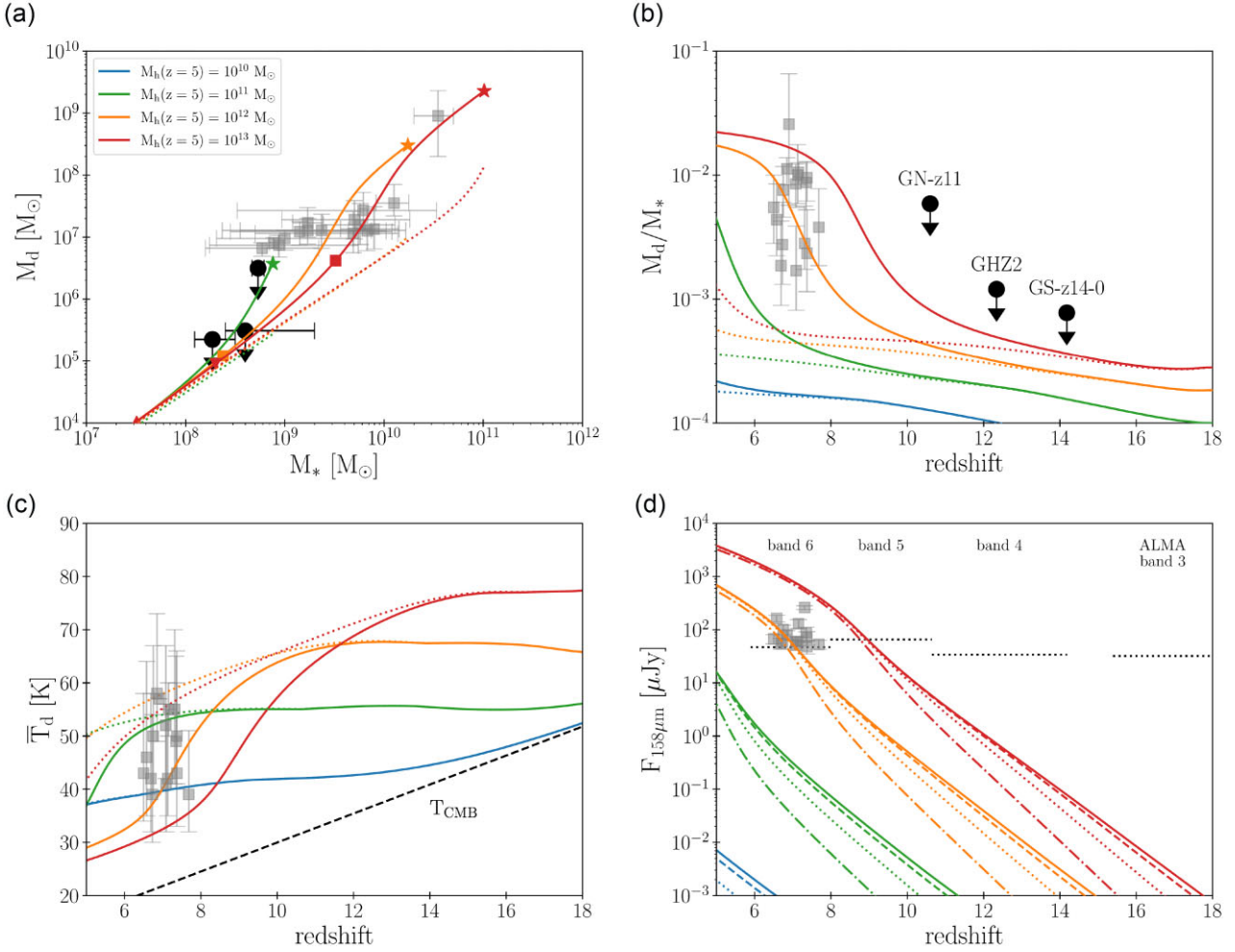
Figure 5. The evolution of dust properties predicted by our model calculations for four haloes that evolve to $M_h(z = 5) = 10^{10}$ (blue), 10^{11} (green), 10^{12} (orange), and $10^{13} M_\odot$ (red). **Panel (a):** The M_*–M_d relation. Solid curves correspond to results with a metal accretion time-scale of $\tau_0 = 5$ Myr, while dotted curves represent $\tau_0 = 50$ Myr. Coloured markers indicate redshifts $z = 18, 15, 13, 10$, and 5, represented by circles, triangles, inverted triangles, squares, and stars, respectively. **Panel (b):** Redshift evolution of the dust-to-stellar mass ratio, M_d/M_*. **Panel (c):** Redshift evolution of the flux-weighted dust temperature of our model galaxies (see equation (30) for the definition). Panels (b) and (c) follow the same line styles as Panel (a). The black dashed line in Panel (c) represents the CMB temperature. **Panel (d):** Redshift evolution of 158 μm dust continuum fluxes. Solid curves show the results from our fiducial model, while dashed, dotted, and dash–dotted curves represent the FIR fluxes calculated by manually reducing the dust UV optical depths by factors of 0.5, 0.1, and 0.01, respectively, to examine the potential effect of mechanisms that alleviate the dust extinction, as discussed in Section 5.1. We also show the 3σ detection limits for one-hour ALMA exposures in Band 3–6 with horizontal dotted lines, indicating that detecting dust continuum from UV-bright galaxies at $z > 10$ with ALMA is extremely challenging. In all panels, our model predictions are compared with the observational data for $z \sim 7$ galaxies, shown as grey squares (Hashimoto et al. 2019; Reuter et al. 2020; Bakx et al. 2021; Sommovigo et al. 2022). In Panels (a) and (b), black circles represent upper limits on the dust mass for the $z > 10$ galaxies, GN-z11 (Fudamoto et al. 2024), GHZ2 (Mitsuhashi et al. 2025), and GS-z14-0 (Carniani et al. 2024a). These limits are derived from the non-detection of dust continuum radiation, assuming a dust temperature of 80 K as analysed in the cited studies.

temperature across the galaxy as follows:

$$\overline{T}_d \equiv \frac{4\pi \int T_d' I_{158} R \mathrm{d}R}{F_{158}}, \qquad (30)$$

where the weighting is based on the dust continuum flux at 158 μm. This flux-weighted temperature is useful for comparing with the observed dust temperature of $z \sim 7$ galaxies, which are usually derived under the assumption of single blackbody radiation.

Fig. 5(c) shows the redshift evolution of $\overline{T}_d$ of our model galaxies. The galaxy hosted by the least massive halo with $M_h(z = 5) \sim 10^{10} M_\odot$ has cold dust with $\overline{T}_d \sim 40$ K at $z \sim 10$, and the temperature remains nearly constant down to $z = 5$. In contrast, galaxies hosted by more massive haloes with $M_h(z = 5) \gtrsim 10^{12} M_\odot$ exhibit higher dust temperature with $\overline{T}_d \sim 65$ K at $z \sim 10$. This hot dust is

a consequence of high SFRs coupled with low dust masses, as $\overline{T}_d$ approximately scales with $(\mathrm{SFR}/M_d)^{1/(4+\beta_d)}$ for optically thick galactic discs, as described by equation (24).

As redshift decreases, the dust temperature in massive galaxies declines rapidly, reaching $\overline{T}_d \sim 30$ K by $z \sim 5$. This decline is primarily driven by a reduction in SFR/M_d due to efficient dust growth, as seen in Figs 5(a) and (b). This is evident from the fact that a longer metal accretion time-scale $\tau_0 = 50$ Myr results in a more gradual decrease in dust temperature, as indicated by the dotted curves in Fig. 5(c). Notably, the predicted $\overline{T}_d$ values of our model galaxies are roughly consistent with the observed dust temperature of $z \sim 7$ galaxies. This consistency suggests that, in the observed galaxies, dust heating by UV radiation becomes less effective as dust mass increases rapidly through metal accretion.
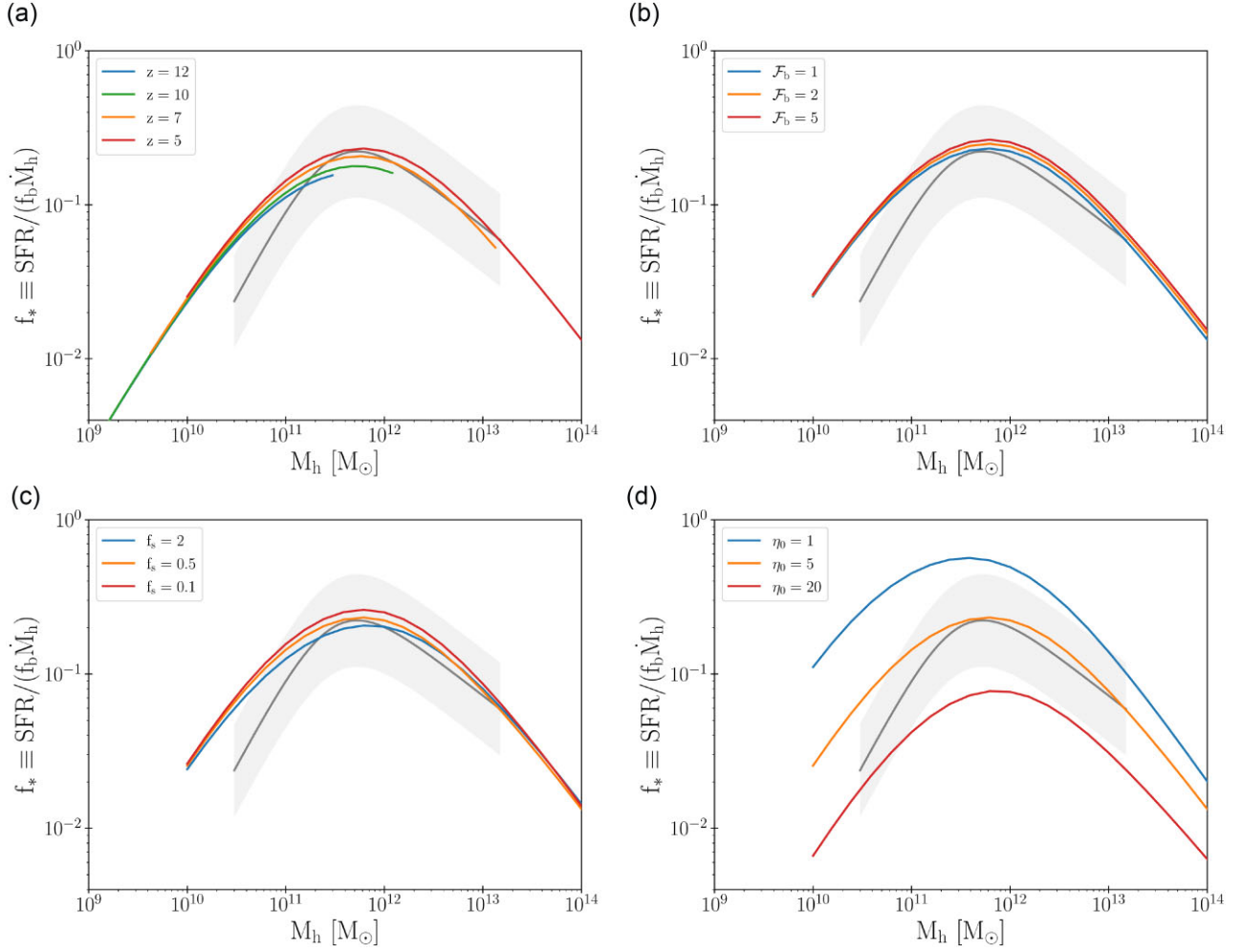
Figure 6. The $f_* - M_h$ relation predicted by our model calculations. **Panel (a)** presents results from our fiducial model at various redshifts. **Panels (b), (c), and (d)** show the effects of varying $\mathcal{F}_b$, f_s, and η_0, respectively. The parameter values corresponding to each coloured curve are noted in the top-left corner of each panel. In all panels, the grey solid curve represents the fitting formula for the observed $f_* - M_h$ relation of $z \sim 2$–7 galaxies, and the shaded region indicates the 2σ scatter in the observational data (Harikane et al. 2022).

Finally, we discuss the detectability of dust continuum radiation from $z > 5$ galaxies. Fig. 5(d) compares the 158 μm dust continuum fluxes predicted by our model with observed fluxes for $z \sim 7$ galaxies (black circles) and the 3σ detection limits for one-hour ALMA exposure in Band 3–6 (dotted horizontal lines). Our results show that dust continuum from galaxies hosted by haloes with $M_h(z = 5) \sim 10^{12}$ (10^{13}) $M_\odot$ is detectable at $z \lesssim 6$ (8). This implies that FIR-bright galaxies observed at $z \sim 7$ are likely associated with such massive dark-matter haloes. Conversely, at $z > 10$, the predicted fluxes from our model galaxies are too faint for detection in the FIR band, consistent with the non-detection of dust continuum in UV-bright galaxies at $z > 10$, such as GN-z11 (Fudamoto et al. 2024), GHZ2 (Zavala et al. 2024; Mitsuhashi et al. 2025), and GS-z14-0 (Schouws et al. 2024; Carniani et al. 2024a).

The non-detectability of FIR emission at $z > 10$ has also been predicted by Ferrara et al. (2024). They proposed that massive galaxies at $z > 10$ are likely to emit hot dust emission with temperatures $T_d \gtrsim 70$ K and a peak wavelength of $\lambda_{peak} \lesssim 40$ μm. As a result, the flux at 158 μm is significantly reduced by a factor of $(\lambda_{peak}/158 \text{ μm})^4$, being undetectable in the ALMA observations. Our detailed model calculations successfully confirm this prediction, offering further

evidence for the challenges of observing dust continuum emission from galaxies at $z > 10$.

4 STAR FORMATION EFFICIENCY

As shown in Section 3, our fiducial model with $\mathcal{F}_b = 1$, $f_s = 0.5$, $\eta_0 = 5$, and $\tau_0 = 5$ Myr successfully explains various properties of $z > 5$ galaxies, including sizes, stellar masses, SFRs, metallicities, and dust contents. These calculations allow us to meaningfully examine star formation activities for high-z galaxies.

We characterize the star formation efficiency (SFE) as $f_* \equiv \text{SFR}/(f_b \dot{M}_h)$ following previous studies (e.g. Harikane et al. 2018, 2022; Inayoshi et al. 2022). Fig. 6(a) shows the $f_* - M_h$ relation at $z \geq 5$, derived from our fiducial model. We find that f_* follows an upward convex trend with M_h, peaking around $M_h \sim 10^{12}$ $M_\odot$, and the peak value is $f_* \sim 0.2$ almost independent of redshift. Our theoretical prediction is in good agreement with the empirical relation for $z \sim 2$–7 galaxies reported by Harikane et al. (2022). Recently, Donnan et al. (2025) have claimed that such a non-evolving SFE is essential to explain the observed UV LFs at $z \sim 6$-13 and the cosmic star formation rates at $z \sim 6$–8. These facts suggest that the $f_* - M_h$ relation remains constant across a fairly wide redshift range.
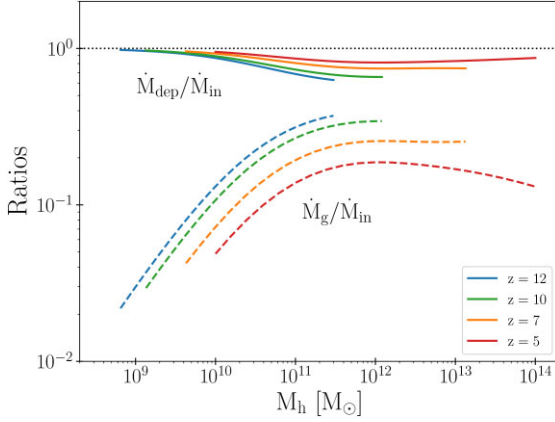
Figure 7. Ratios of $\dot{M}_{\rm dep}/\dot{M}_{\rm in}$ (solid curves) and $\dot{M}_{\rm g}/\dot{M}_{\rm in}$ (dashed curves) as functions of halo mass $M_{\rm h}$, derived from our fiducial model. Blue, green, orange, and red curves represent the results at $z = 12$, 10, 7, and 5, respectively.

Additionally, we examine how f_* depends on the three parameters $\mathcal{F}_{\rm b}$, $f_{\rm s}$, and η_0 in Figs 6(b)–(d). We find that while higher $\mathcal{F}_{\rm b}$ and lower $f_{\rm s}$ results in slightly higher f_* at any given $M_{\rm h}$, the variations are minimal. This trend is consistent with what we observed in the M_*–SFR relation in Fig. 4. In contrast, f_* exhibits a much stronger dependence on η_0, increasing in inverse proportion to η_0, while the overall shape of the f_*–$M_{\rm h}$ relation remains unchanged. These results suggest that the SFE within a galaxy is predominantly governed by the total mass lost via outflows, rather than by the local star formation law or the spatial distribution of gas.

These trends in the f_*–$M_{\rm h}$ relation can be understood as follows. By integrating equation (1) over the entire galactic disc, the time evolution of the total gas mass is given by,

$$\dot{M}_{\rm g} = \dot{M}_{\rm in} - \dot{M}_{\rm dep} , \quad \dot{M}_{\rm dep} \equiv {\rm SFR} + \dot{M}_{\rm out} - \dot{M}_{\rm ret} , \quad (31)$$

where $\dot{M}_{\rm dep}$ represents the net gas depletion rate including star formation, outflows, and mass return from stars. Fig. 7 compares the three terms in equation (31), derived from our fiducial model. We find that the ratio of $\dot{M}_{\rm dep}/\dot{M}_{\rm in}$ ($\dot{M}_{\rm g}/\dot{M}_{\rm in}$) increases (decreases) toward lower redshifts. This redshift evolution arises because the relative importance of cosmological gas inflows declines with time, as $\dot{M}_{\rm in} \propto (1 + z)^{2.5}$. At each redshift, $\dot{M}_{\rm dep}/\dot{M}_{\rm in}$ ($\dot{M}_{\rm g}/\dot{M}_{\rm in}$) reaches a minimum (maximum) at $M_{\rm h} \sim 10^{12}$ M$_\odot$. This behavior is also explained as, at this halo mass, inflows are more efficient relative to gas depletion, primarily driven by outflows, reflecting the assumed halo mass dependencies of $\epsilon_{\rm in}$ and η (see equations 13 and 15).

It is worth noting here that $\dot{M}_{\rm g}/\dot{M}_{\rm in}$ remains below ~ 40 per cent even at z = 12. Consequently, $\dot{M}_{\rm dep}/\dot{M}_{\rm in}$ is approximately unity across all redshifts and halo mass, indicating that our model galaxies evolve in a quasi-steady state, where the gas depletion approximately balances with the gas supply. Such equilibrium is a natural outcome of a self-regulating mechanism. When gas supply exceeds gas depletion in a galaxy, the increased gas mass triggers enhanced star formation and subsequent outflows, which in turn accelerates gas depletion. Conversely, when gas depletion surpasses gas supply, the galaxy depletes its gas reservoir, leading to reduced SFRs. As a result, galaxies naturally settle into an equilibrium state. This self-regulation also explains the weak dependence of f_* on $\mathcal{F}_{\rm b}$ and $f_{\rm s}$. Although higher $\mathcal{F}_{\rm b}$ and lower $f_{\rm s}$ enhance local star formation rates $\dot{\Sigma}_{\rm sf}$, this accelerates gas depletion within the galaxy, preventing a sustained increase in the global SFR.

Then, by assuming $\dot{M}_{\rm g} \sim 0$ in equation (31), we can approximate f_* as,

$$f_* \equiv \frac{\rm SFR}{f_{\rm b} \dot{M}_{\rm h}} \sim \frac{\epsilon_{\rm in}}{1 - \mathcal{R} + \eta} , \quad (32)$$

where $\mathcal{R} \equiv \dot{M}_{\rm ret}/{\rm SFR} \sim 0.5$ denotes the return mass fraction from stellar evolution. This yields $f_* \sim 0.18$ for $M_{\rm h} = 10^{11}$ M$_\odot$ and $\eta_0 = 5$ as in our fiducial model. This expression highlights that f_* is primarily governed by $\epsilon_{\rm in}$ and η. Specifically, our model predicts

$$f_* \sim \begin{cases} \eta^{-1} \propto M_{\rm h}^{1.1}, & (M_{\rm h} \ll 10^{11}~{\rm M}_\odot) \\ \epsilon_{\rm in}/(1 - \mathcal{R}) \propto M_{\rm h}^{-1} & (M_{\rm h} \gg 10^{12}~{\rm M}_\odot) . \end{cases} \quad (33)$$

These trends reflect the underlying physics of viral shocks and supernova-driven outflows, as assumed in our functional forms of $\epsilon_{\rm in}$ and η (see Section 2.2). Furthermore, if $\epsilon_{\rm in}$ and η are nearly independent of redshifts, our formulation naturally explains the weak redshift evolution of f_* observed for $z < 7$ galaxies (Harikane et al. 2018, 2022; Donnan et al. 2025). Conversely, if a higher f_* is required to match cosmic SFR density at $z \gtrsim 10$, as suggested by Harikane et al. (2023), this would imply a need to reduce η, given that further increasing $\epsilon_{\rm in}$ beyond unity is unphysical. We will explore this point more explicitly in Sections 5.3 and 5.4. Additionally, our model overestimates f_* at $M_{\rm h} < 10^{11}$ M$_\odot$ compared to the observed relation. According to equation (33), this tension is alleviated by increasing η in low-mass haloes, namely by adopting a steeper power-law index in the first term of equation (15). This finding provides an important implication for outflow driving mechanisms, particularly in dwarf galaxies.

Thus, the f_*–$M_{\rm h}$ relation reflects the quasi-steady evolution of galaxies and encapsulates the nature of galactic inflows and outflows. Recently, Yung, Somerville & Iyer (2025) constrained the functional form of the f_*–$M_{\rm h}$ relation by fitting to observed UV LFs at various redshifts. Their derived f_*–$M_{\rm h}$ relation at $z \sim 12$ is generally in good agreement with the prediction from our fiducial model but suggests that a peak f_* value is approximately twice as high. According to equation (33), their result corresponds to $\eta_0 \sim 2$ at $z = 12$. However, as shown in Fig. 4, our model disfavors such a low mass-loading factor, as it fails to reproduce the observed low metallicities of $z > 10$ galaxies. Furthermore, in Section 5.1, we demonstrate that our model can successfully reproduce the observed UV LF at $z = 12$ when dust attenuation is assumed to be negligible.

We note that the quasi-steady behavior in our model may stem from the assumption of continuous dark matter halo assembly history given by equation (11). In reality, galaxies temporarily deviate from the quasi-steady state, as episodic gas inflows driven by galaxy mergers lead to intermittent star formation and outflows. Nevertheless, we suggest that, over longer time-scales, galaxies tend to evolve toward a balance between gas supply and depletion, resulting in a small statistical scatter and weak redshift dependence in the observed f_*–$M_{\rm h}$ relation. To fully understand the impact of bursty star formation histories on the statistical properties of f_*, it is crucial to extend our model to incorporate realistic mass assembly histories.

5 DISCUSSION

5.1 UV luminosity functions and implications for dust attenuation

Our model predicts the intrinsic and dust-attenuated UV magnitudes of galaxies as functions of host dark-matter halo masses and redshifts.

By combining these relations with the Sheth–Tormen dark-matter halo mass function (Sheth & Tormen 2002), we can construct UV LFs at any redshifts. Fig. 8 a shows our theoretical UV LFs at $z = 12$ as well as an observed UV LF inferred with spectroscopically confirmed galaxy samples by Harikane et al. (2025). For comparison, we also show LFs calculated assuming constant SFEs of $f_* = 100$ per cent, 10 per cent, and 1 per cent. Notably, our intrinsic LF, shown by the red curve, broadly agrees with the observed LF over the range from $M_{\rm UV} \sim -23$ mag to -17 mag. This agreement arises from the fact that the faint-end and bright-end galaxies are hosted by haloes with $M_{\rm h} \sim 10^{10}$ M$_\odot$ and 10^{11} M$_\odot$ and form stars with SFEs of $f_* \sim 3$ per cent and 10 per cent, respectively, as shown in Fig. 6(a).

We note, however, that the dust-attenuated LF, shown by the blue solid curve in Fig. 8(a), exhibits significant suppression at $M_{\rm UV} \lesssim -20$ mag compared to the intrinsic LF. This suppression arises from high optical depths of these galaxies, $\tau_{1500} \gtrsim 10$, which results from high surface gas densities of $\Sigma_{\rm g} \gtrsim 10^4$ M$_\odot$ pc^{-2} with dust-to-gas mass ratios of $D/D_{\rm MW} \sim 0.01$ (see Appendix C). Thus, our model appears to overestimate the optical depths and, consequently, the effect of dust attenuation. To address this issue, we examine how much the dust optical depth needs to be reduced to reproduce the observed UV LF. The different blue curves in Fig. 8(a) show the UV LFs with τ_{1500} manually reduced by factors of 0.5, 0.1, and 0.01. This analysis reveals that a $\gtrsim 90$ per cent reduction in τ_{1500} is necessary for our model to be consistent with observations. Indeed, such low values of τ_{1500} have also been invoked to explain extremely blue UV colours of $z \gtrsim 10$ galaxies (e.g. Topping et al. 2022, 2024; Cullen et al. 2024; Morales et al. 2024; Yanagisawa et al. 2024).

We also conduct a similar analysis for the UV LFs at $z = 7$, as shown in Fig. 8(b). The intrinsic UV LF at this redshift exceeds the observed one by approximately an order of magnitude near the bright end, suggesting a need for non-negligible dust extinction to reconcile the discrepancy with observations. However, the dust-attenuated UV LF (blue solid curve) falls significantly below the observed one at $M_{\rm UV} \lesssim -20$ mag. This sharp decline at the bright end is more pronounced than at $z = 12$ due to the rapid increase of the dust-to-stellar mass ratio caused by efficient metal accretion onto dust grains, which occurs around $z \sim 10$ (see Appendix C). Then, the different blue curves in Fig. 8(b) suggest that to explain the observed galaxy abundance at $M_{\rm UV} \sim -23$ mag, τ_{1500} needs to be reduced by at least a factor of ~ 0.01. Even with such a significant reduction, however, this model fails to replicate the overall slope of the bright end of the observed UV LF. Thus, at $z = 7$, the discrepancy between the model prediction and the observation is more pronounced than at $z = 12$, highlighting the critical importance of exploring dust physics across a wide redshift range.

It is also worth noting that if UV attenuation is suppressed by any mechanisms, it can reduce the energy absorbed by dust, thereby dimming the dust continuum radiation. Consequently, the FIR fluxes derived using the original optical depths (solid curves in Fig. 5d) would be regarded as optimistic upper limits. To demonstrate this, Fig. 5(d) also presents FIR fluxes assuming the reduced optical depths, shown by different line styles. We find that a reduction in τ_{1500} up to ~ 90 per cent has minimal impact on FIR fluxes, as the reduced optical depths remain large enough for substantial UV photon absorption. In contrast, when τ_{1500} is reduced by 99 per cent, the FIR fluxes drop by approximately an order of magnitude at $z \gtrsim 10$. This effect becomes less pronounced at lower redshifts, where the original optical depths are higher. This analysis suggests that detecting the FIR dust continuum in $z > 10$ galaxies could be challenging, especially if UV photons escape more efficiently than anticipated by our model calculations.

5.2 How do galaxies avoid significant dust attenuation?

Here, we explore potential mechanisms that could mitigate the effects of dust attenuation without altering the fundamental characteristics of our model galaxies. In the following discussion, we consider the one-zone averaged dust optical depth given by:

$$\tau_{1500} \sim \kappa_{1500} \frac{D M_{\rm g}}{2\pi R_{\rm eff}^2}$$

$$\sim 34.6 \left(\frac{\kappa_{1500}}{1.26 \times 10^5 \, {\rm cm}^2 {\rm g}^{-1}} \right) \left(\frac{M_{\rm g}}{10^{10} \, {\rm M}_\odot} \right)$$

$$\times \left(\frac{R_{\rm eff}}{500 \, {\rm pc}} \right)^{-2} \left(\frac{D/D_{\rm MW}}{0.01} \right) , \qquad (34)$$

where the reference values of $M_{\rm g}$, $R_{\rm eff}$, and D are representative of bright-end galaxies at $z \sim 12$. A straightforward approach to reduce τ_{1500} is to decrease either D or $M_{\rm g}$. Our model can achieve this by supposing more gas and dust evacuation from galaxies with higher values of η_0. However, further increasing η_0 would lead to gas depletion in galaxies, making it difficult to reproduce the M_*–SFR–Z relation of $z > 5$ galaxies. Furthermore, excessively reducing D could conflict with the presence of dust-rich galaxies observed at $z \sim 7$. Therefore, we disfavor this approach as an effective way to reduce τ_{1500}. Alternatively, we discuss three possibilities in the following.

5.2.1 Dust displacement

The first possibility is that dust is displaced to large ($\sim$kpc) scales by radiation-driven outflows. Fiore et al. (2023) have proposed that in $z > 10$ galaxies, radiation pressure on dust grains is usually strong enough to drive substantial dusty outflows (see also Fukushima, Yajima & Omukai 2018; Ferrara et al. 2023). While these dusty outflows are likely still gravitationally bound by the galaxy and expected to eventually return to the galactic disc, they can temporarily extend the spatial distribution of dusty gas relative to the stellar component (Ziparo et al. 2023; Ferrara et al. 2024). If the effective radius of dusty gas ($R_{\rm eff,d}$) increases to $R_{\rm eff,d} \gtrsim 5 \, R_{\rm eff}$, τ_{1500} decreases by $\gtrsim 25$. This reduction is sufficient to reconcile the discrepancy between the UV LF predicted by our model and the observed one at $z \sim 12$.

A potential concern with this scenario is that substantial dust removal from the main galaxy body shuts down star formation, leading to a decline in UV luminosity of the galaxy. To sustain the UV brightness, it is crucial that dusty outflows return to the galactic disc and re-activate star formation before massive stars with lifetimes of $\lesssim 100$ Myr cease producing UV radiation.

Indeed, the galaxy GS-z14-0 at $z = 14.32$, characterized by its bright UV luminosity ($M_{\rm UV} = -20.81$ mag), and low dust attenuation ($A_V = 0.31$), may currently be in a 'mini-quenching' phase of star formation, as suggested from the absence of strong emission lines (Carniani et al. 2024b; Ferrara 2024b). If star formation is not reactivated within ~ 100 Myr, the galaxy's UV luminosity is expected to decline below the *JWST* detection limit due to the depletion of its massive stars.

To assess whether dusty outflows can return to the galactic disc within this time-scale, we estimate the free-fall time-scale for dusty gas extending beyond the UV half-light radius by a factor of $\chi_{\rm d}$, i.e. $R_{\rm eff,d} = \chi_{\rm d} R_{\rm eff}$, which is given by

$$\tau_{\rm ff} \sim \sqrt{\frac{R_{\rm eff,d}^3}{G \, M_{\rm g}}} \sim 20 \, {\rm Myr} \left(\frac{M_{\rm g}}{10^{10} \, {\rm M}_\odot} \right)^{-1/2} \left(\frac{R_{\rm eff}}{500 \, {\rm pc}} \right)^{3/2} \left(\frac{\chi_{\rm d}}{5} \right)^{3/2} .$$

$$\qquad (35)$$
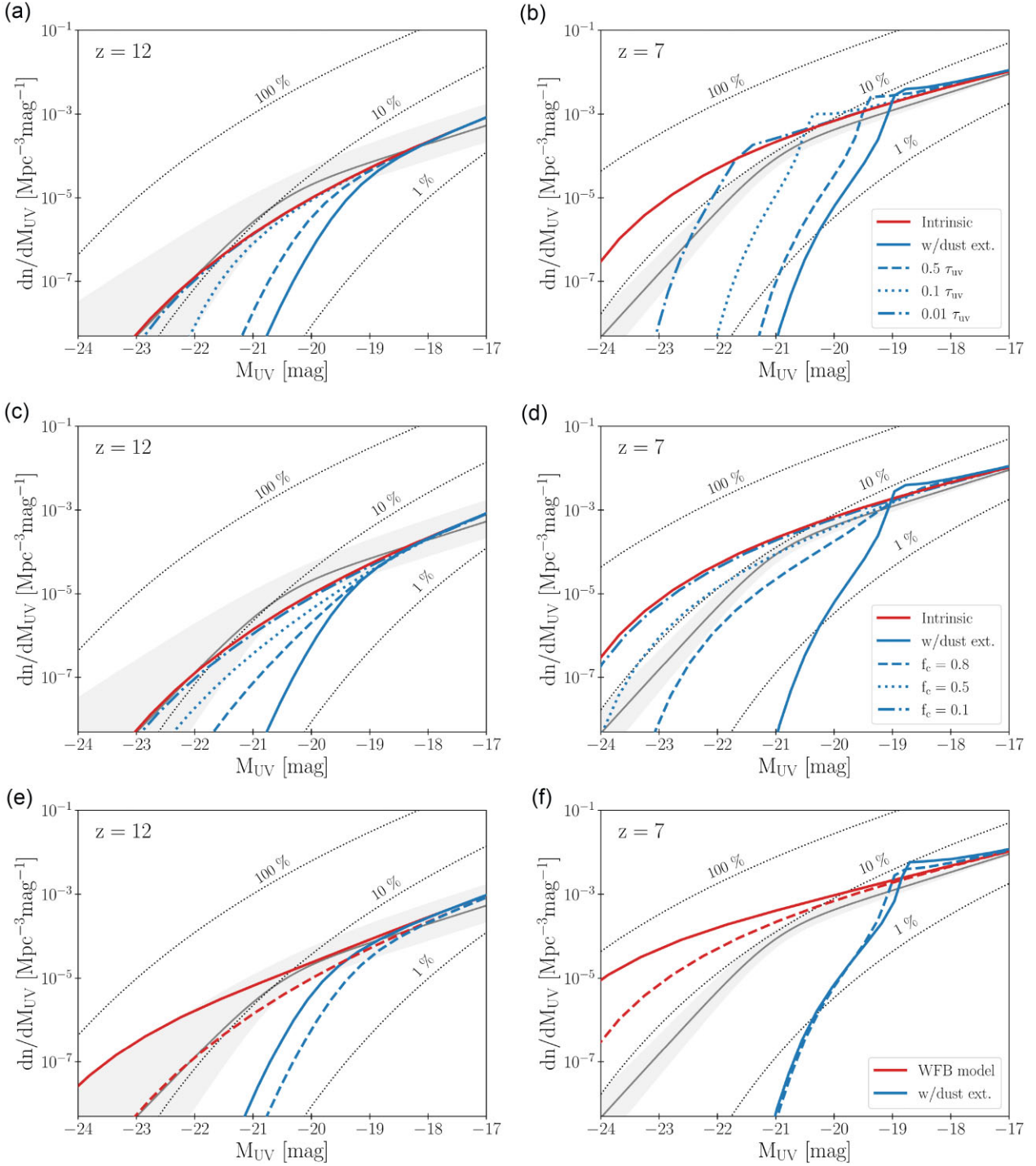
Figure 8. Panels (a) and (b) shows the UV LFs at $z = 12$ and 7, respectively, derived from our fiducial model. The red solid curve represents the intrinsic UV LF, while the blue solid curve indicates the dust-attenuated UV LF. To highlight the impact of dust extinction, dust-attenuated UV LFs with optical depths reduced by factors of 0.5, 0.1, and 0.01 are shown as the blue dashed, dotted, and dash–dotted curves, respectively. **Panels (c) and (d)** present the same quantities as panels a and b, respectively, but here the blue dashed, dotted, and dash–dotted curves represent UV LFs calculated for different dust covering fractions of $f_c = 0.8$, 0.5, and 0.1, respectively (see Section 5.2.3 for the definition of f_c). **Panels (e) and (f)** also correspond to panels (a) and (b), respectively, but the red and blue solid curves now show the intrinsic and dust-attenuated UV LFs predicted by the weak feedback model, while the dashed curves indicate the corresponding results from the fiducial model for comparison. In all panels, the observed UV LFs and their 1σ uncertainties presented by Harikane et al. (2025) are depicted by the gray curves and shaded regions, Black dotted curves correspond to UV LFs predicted assuming constant SFEs of $f_* = 100$ per cent, 10 per cent, and 1 per cent.

For bright-end galaxies at $z \sim 12$, this estimated time-scale is generally shorter than the lifetime of massive stars. This suggests that even if star formation is temporarily halted by significant dust removal, it can resume through gas circulation before the UV luminosity declines noticeably. This fact supports the plausibility of this dust displacement scenario.

5.2.2 Large grain size

The second possibility to reduce τ_{1500} is to decrease κ_{1500} by assuming large dust grains with sizes of 0.1–$1\,\mu$m. This scenario would be plausible in the early universe, where SNe are the dominant contributors to dust production, and small grains are preferentially destroyed by reverse shock in SN ejecta (Nozawa et al. 2007; Asano et al. 2013; Hirashita & Aoyama 2019). If the typical grain size, a_g, is sufficiently larger than the reference UV wavelength ($\lambda = 0.15\,\mu$m), the absorption cross-section can be approximated as (Ferrara et al. 2024),

$$\kappa_{1500}^{\mathrm{large}} \sim \frac{\pi a_\mathrm{g}^2}{\frac{4\pi}{3}\delta_\mathrm{g}a_\mathrm{g}^3} \sim 5085\,\mathrm{cm}^2\mathrm{g}^{-1}\left(\frac{a_\mathrm{g}}{0.5\,\mu\mathrm{m}}\right)^{-1}, \tag{36}$$

where $\delta_\mathrm{g} = 2.95$ g cm^{-3} is the material density of silicate grains, which are preferentially produced by SNe. Thus, large grains with $a_\mathrm{g} = 0.5\,\mu$m yield $\kappa_{1500}^{\mathrm{large}} \sim 0.04\,\kappa_{1500}$, and the resulting τ_{1500} is of the same order as for the dust displacement scenario. It is worth noting that a flat extinction curve, which arises due to such large grain sizes at wavelength shorter than a_d, has been reported in $z > 6$ *JWST*-detected galaxies (Markov et al. 2024, 2025). Such flat attenuation curves would also be necessary to explain the blue excess slope observed in Little Red Dots, which are promising candidates for $z > 5$ active galactic nuclei (Li et al. 2024a). Thus, large dust grains would be a promising scenario for understanding various physical properties of galaxies in the early universe.

5.2.3 Dust-to-star segregation

Finally, we consider the third possibility: the spatial segregation of dust from young massive stars within the galactic disc. Hydrodynamic simulations suggest that during the final stages of stellar cluster formation, stellar feedback clears internal gas and dust, leaving young stars within rarefied bubbles (e.g. Hu 2019; Sugimura et al. 2024). This process allows a substantial fraction of UV light to escape from the star-forming regions effectively. Indeed, recent galactic-scale simulations demonstrate that spatial segregation of dust from young stars reduces the overall dust attenuation experienced by galaxies (e.g. Narayanan et al. 2018; Vijayan et al. 2024). Unlike the dust displacement scenario discussed earlier, this mechanism allows substantial amounts of dust to remain in the galactic disc, potentially creating some highly obscured regions. Consequently, the nature of dust attenuation predicted under this scenario can differ significantly from those predicted in the first two scenarios. To explore this effect, we introduce a parameter f_c, defined as the fraction of young massive stars embedded in optically thick gas. Assuming that UV photons from the remaining $(1 - f_\mathrm{c})$ fraction of stars are completely unobscured, the observed UV luminosity can be expressed as,

$$L_\mathrm{UV}^{\mathrm{obs}} = (1 - f_\mathrm{c})L_\mathrm{UV}^{\mathrm{int}} + f_\mathrm{c} f_\mathrm{esc}(\tau_{1500}')L_\mathrm{UV}^{\mathrm{int}}, \tag{37}$$

where $\tau_{1500}' \equiv \tau_{1500}/f_\mathrm{c}$ is the effective dust optical depth in the obscured regions, ensuring the total dust mass remains unchanged.

Figs 8(c) and (d) shows UV LFs at $z = 12$ and 7, respectively, for different values of f_c. We find that the model with $f_\mathrm{c} \sim 0.1$ generally agrees with the observation at $z = 12$, whereas $f_\mathrm{c} \sim 0.5$ is favourable for explaining the UV LF at $z = 7$. In contrast to models with reduced τ_{1500} in Figs 8(a) and (b), the dust segregation model predicts a more gradual decline at the bright end of the UV LF, as even massive galaxies with $\tau_{1500} > 100$ allow some UV photons to escape. Interestingly, the f_c values required to fit the observations decrease from $z = 12$ to 7. This trend likely reflects the increasing mass of bright-end galaxies toward lower redshifts, which reduces the impact of stellar feedback on the ISM structure due to their deeper gravitational potential wells.

Previous studies have, however, argued that dust segregation enhances FIR fluxes, potentially conflicting with the observed non-detection of dust continuum in $z > 10$ galaxies. Ferrara et al. (2022) demonstrated that in the absence of dust segregation, FIR fluxes have an upper limit for given UV fluxes and dust extinction. A significant excess of FIR fluxes above this theoretical upper limit would indicate substantial dust-to-star segregation in galaxies. Following this argument, Ziparo et al. (2023) suggested that $z > 10$ galaxies are unlikely to have strong dust segregation, as their intrinsic FIR fluxes inferred from the non-detection have to be far below the theoretical upper limits. Furthermore, it is highly ambiguous whether significant segregation ($f_\mathrm{c} \sim 0.1$) is achievable in the bright-end galaxies at $z > 10$, particularly given their very compact nature. Their high surface densities ($\Sigma_\mathrm{g} \sim 10^4\,\mathrm{M}_\odot\mathrm{pc}^{-2}$) could hinder effective bubble formation by stellar feedback (e.g. Grudić et al. 2018; Dekel et al. 2023). Thus, whether dust segregation can self-consistently explain the observed properties of $z > 10$ galaxies remains an open question. Addressing this issue requires high-resolution hydrodynamic simulations capable of resolving sub-pc structures in dusty ISM while incorporating both UV and FIR radiation transfer in galaxies.

5.3 Cosmic star formation rate density

In Section 4, we find that the f_*–M_h relation is generally preserved across a wide redshift range as a consequence of quasi-steady galaxy evolution. We examine whether the non-evolving f_*–M_h relation is consistent with recent measurements of cosmic SFR densities (CSFRDs) for $z > 8$ galaxies. CSFRDs are calculated as follows:

$$\rho_{\mathrm{SFR}} = \int \mathrm{SFR}\frac{\mathrm{d}n}{\mathrm{d}M_{\mathrm{UV}}}\mathrm{d}M_{\mathrm{UV}}$$
$$= \int f_* f_\mathrm{b}\dot{M}_\mathrm{h}\frac{\mathrm{d}n}{\mathrm{d}M_\mathrm{h}}\mathrm{d}M_\mathrm{h}, \tag{38}$$

where the integration is typically carried out down to $M_{\mathrm{UV}}^{\mathrm{lim}} = -17$ mag or up to the corresponding halo mass (e.g. Madau & Dickinson 2014; Oesch et al. 2014; Finkelstein et al. 2015; McLeod, McLure & Dunlop 2016). Harikane et al. (2022) calculated equation (38) under the assumption of a non-evolving f_*–M_h relation observed at $z \sim 2$–7 and demonstrated that CSFRDs decline rapidly at $z \gtrsim 8$ following $\rho_{\mathrm{SFR}} \propto 10^{-0.5(1+z)}$.

We evaluate CSFRDs using our calculation results. In this analysis, we neglect the effects of dust attenuation for comparison with observed CSFRDs that are corrected for dust extinction. Fig. 9 compares CSFRDs predicted by our fiducial model (red curve) with the theoretical result from Harikane et al. (2022) (grey curve) and recent observational measurements at $z \gtrsim 8$. Our prediction is in good agreement with the model of Harikane et al. (2022), which is expected since the f_*–M_h relation in our model is generally consistent with their results (see Fig. 6a). Additionally, our model aligns well with recent observational data up to $z \sim 13$. However,
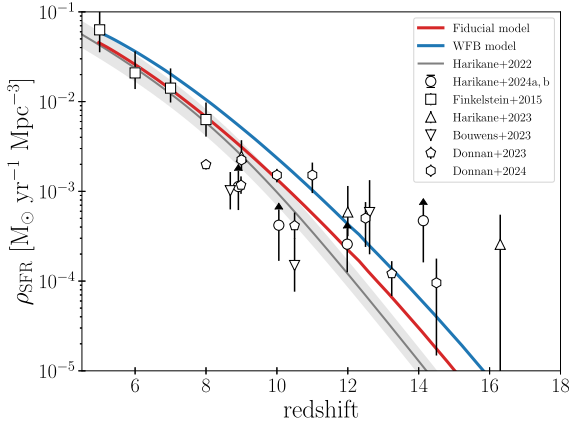
Figure 9. The CSFRDs predicted by our fiducial model are shown by the red curve. For comparison, the CSFRDs obtained by the weak feedback model are depicted by the blue curve. The grey curve and shaded region represent the fitting formula to observed CSFRDs at $z \lesssim 7$ from Harikane et al. (2022) and its 1σ (0.15 dex) scatter, respectively. Additionally, various open symbols indicate observed CSFRDs at $z \sim 5$–16 (Finkelstein et al. 2015; Bouwens et al. 2023; Donnan et al. 2023, 2024; Harikane et al. 2023).

at $z \gtrsim 14$, our prediction tends to underestimate CSFRDs compared to observations, implying that SFEs in the early universe must be a few times greater than the f_*–M_h relation predicted by our model. One potential explanation for this discrepancy is the feedback-free galaxy evolution scenario, proposed by Dekel et al. (2023). This scenario supposes that in extremely early galaxies, high gas density results in a short free-fall time for gas clouds, causing rapid star formation. As a result, a large fraction of gas turns out stars before the onset of supernovae, and mass loss by galactic outflows can be negligible, i.e. $\eta \ll 1$. According to equation (32), such conditions yield a high SFE of $f_* \sim 1$. Thus, if feedback-free galactic evolution is common at $z \gtrsim 14$, it could explain the high CSFRDs observed at these redshifts. However, we claim that this extremely efficient star formation must cease before $z \sim 12$ to maintain the excellent agreement between our model predictions and observations across multiple properties, such as metallicities, UV LFs, and CSFRDs. In the following subsection, we explicitly examine the potential effects of feedback-free evolution on observed properties of high-z galaxies.

5.4 Weak-feedback scenario

Our fiducial model that assumes the KS law with $\mathcal{F}_\mathrm{b} = 1$ and a high mass loading factor of $\eta_0 = 5$ likely provides a conservative prediction on SFEs of $z > 5$ galaxies. To explore a more optimistic scenario, we consider a weak-feedback (WFB) model, where the SFR per unit gas mass increases and the mass loading factor decreases in environments of higher gas densities. This model is motivated by radiation hydrodynamics simulations of Fukushima & Yajima (2021) showing a sharp rise in the SFR per cloud when the cloud surface density exceeds a critical threshold, Σ_cr. To implement this effect in our model, we express the boost factor $\mathcal{F}_\mathrm{b}$ in equation (10) as follows:

$$\mathcal{F}_\mathrm{b} = 1 + \frac{\mathcal{F}_{\mathrm{b},0} - 1}{1 + \exp(-f_\mathrm{cr})} \,, \quad f_\mathrm{cr} = 5\frac{\Sigma_\mathrm{g} - \Sigma_\mathrm{cr}}{\Sigma_\mathrm{cr}} \,. \tag{39}$$

This expression refers to equations (16) and (17) of Fukushima & Yajima (2021) and leads to $\mathcal{F}_\mathrm{b} \sim 1$ at $\Sigma_\mathrm{g} \ll \Sigma_\mathrm{cr}$ and $\mathcal{F}_\mathrm{b} \sim \mathcal{F}_{\mathrm{b},0}$

at $\Sigma_\mathrm{g} \gg \Sigma_\mathrm{cr}$. We set $\mathcal{F}_{\mathrm{b},0} = 10$ according to spatially-resolved SFRs measured in $z > 5$ galaxies (Vallini et al. 2024). We here assume $\Sigma_\mathrm{cr} = 10^3$ $M_\odot \mathrm{pc}^{-2}$, above which the gravitational potential of the clouds is considered to be deep enough to confine gas accelerated by supernova momentum deposition (e.g. Grudić et al. 2018, 2020; Byrne et al. 2023). For consistency with the increased SFRs, we depress the mass loading factor, scaling it by a factor of $(1 + \Sigma_\mathrm{g}/\Sigma_\mathrm{cr})^{-1}$.

Our WFB model is modest compared to the feedback-free model proposed by Dekel et al. (2023), which assumes the complete absence of outflows in star-forming regions with gas densities larger than 10^3 cm^{-3}. They suppose that, in such dense environments, the free-fall time of gas clouds is significantly shorter than the lifetimes of massive stars, allowing a substantial fraction of gas to be converted into stars before supernova-driven feedback operates effectively. Thus, if our WFB model already overpredicts key quantities, such as SFRs, stellar masses, gas metallicities, and dust masses, relative to observational constraints, the feedback-free model would inevitably lead to even larger discrepancies.

Figs 10(a)–(c) present some results from the WFB model, showing the SFR, metallicity, and dust mass as functions of stellar mass. Compared to the fiducial model, the WFB model predicts higher SFRs, particularly in massive haloes with $M_\mathrm{h}(z = 5) \gtrsim 10^{12}$ $M_\odot$, where disc surface densities are sufficiently higher than $\Sigma_\mathrm{cr} = 10^3$ $M_\odot \,\mathrm{pc}^{-2}$. For these massive haloes, metallicities are elevated by a few 10 per cent, compared to the fiducial model, owing to the suppression of metal evacuation. This enhanced metallicity accelerates dust mass growth via metal accretion, leading to dust masses a few times higher than those in the fiducial model.

The impact of weak feedback on SFEs is examined in Fig. 10(d). The f_*–M_h relation in the WFB model is systematically shifted upward compared to observations. In particular, the peak SFE reaches $f_* \sim 0.6$, which is approximately three times greater than the observed value. Moreover, the redshift dependence of the f_*–M_h relation is more pronounced than in the fiducial model. This is because, in the WFB model, the mass loading factor evolves over time in response to changing surface gas densities. For comparison, we note that the feedback-free model predicts $f_* \gtrsim 0.5$ for all haloes with $M_\mathrm{h} \gtrsim 10^{10}$ $M_\odot$ at $z \sim 12$ (Li et al. 2024b), although our model provides such high SFEs only for haloes with $M_\mathrm{h} \sim 10^{11-12}$ $M_\odot$.

Figs 8(e) and (f) show that the elevated SFEs in the WFB model extend the bright end of the intrinsic UV beyond those predicted by the fiducial model. However, the dust-attenuated UV LFs remain similar to those in the fiducial model, indicating that the WFB model leads to stronger dust attenuation due to efficient dust growth facilitated by suppressed metal evacuation. Therefore, even under the WFB scenario, mitigating dust attenuation remains crucial to describe the galaxy evolution at such high redshifts.

Finally, we examine the CSFRD predicted by the WFB model, which is shown by the blue curve in Fig. 9. The WFB model generally reproduces the observed CSFRDs at $z \sim 12$–14. At later epochs, the CSFRDs of the WFB model gradually converge towards those of the fiducial one but remain higher by about a factor of two even at $z = 5$. This excess arises because, in our model, massive galaxies hosted by haloes with $M_\mathrm{h} \gtrsim 10^{11}$ $M_\odot$ retain high surface gas densities of $\Sigma_\mathrm{g} \gtrsim 10^3$ $M_\odot \,\mathrm{pc}^{-2}$ even at $z < 10$, resulting in the regulated stellar feedback. Notably, the WFB model slightly overestimates the CSFRDs, compared to observations at $5 \lesssim z \lesssim 10$. There are two possible explanations for this discrepancy. First, the CSFRDs derived from the UV LFs of galaxies may be underestimated due to observational uncertainties in dust extinction correction. Indeed, several studies have reported CSFRDs at $z > 5$ that are higher by a
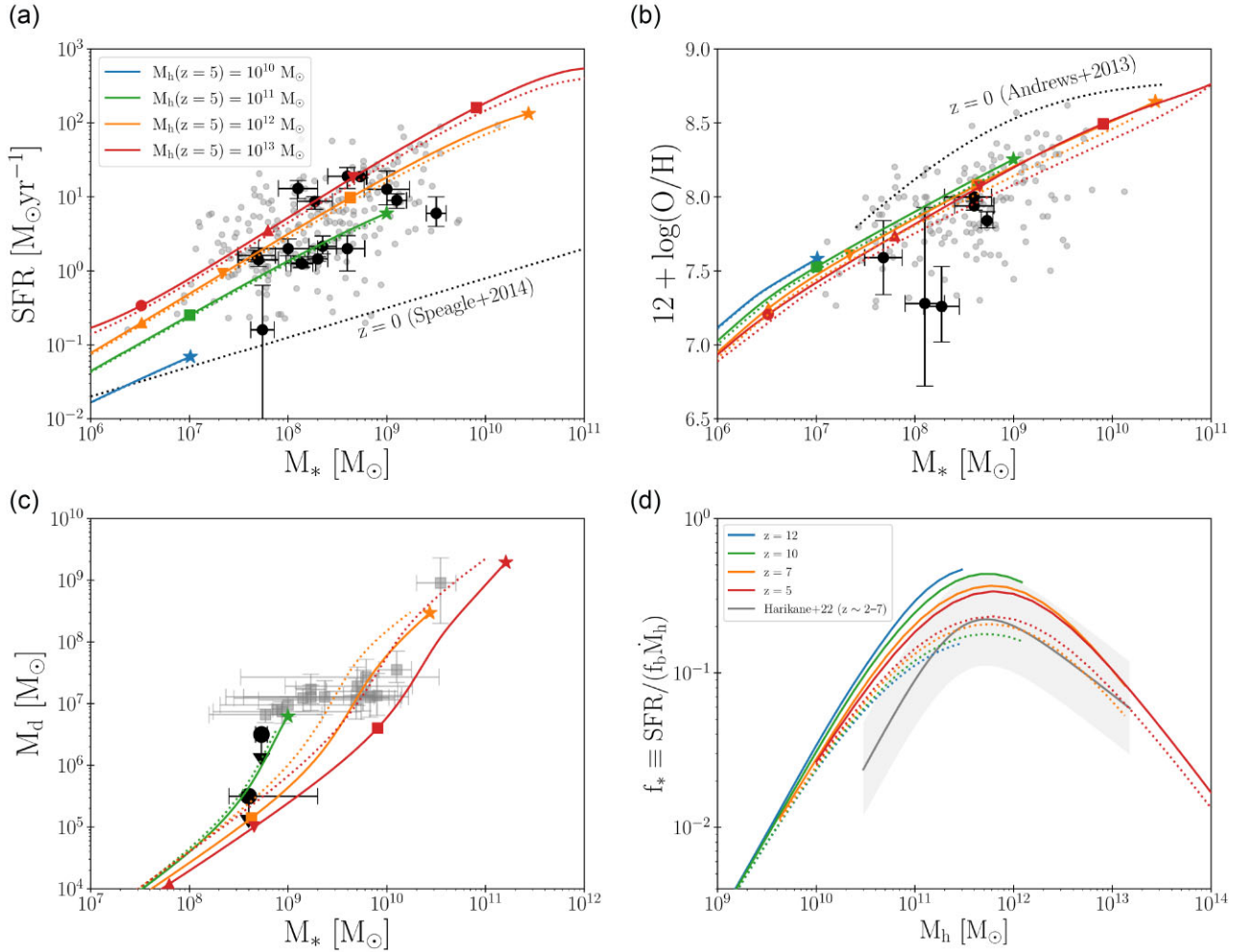
Figure 10. Results from the weak feedback model. **Panel (a):** The M_*–SFR relation, corresponding to the top-left panel of Fig. 4. **Panel (b):** The M_*–$12 + \log(O/H)$ relation, corresponding to the top-middle panel of Fig. 4. **Panel (c):** The M_*–M_d relation, corresponding to Fig. 5(a). **Panel (d):** The f_*–M_h relation, corresponding to Fig. 6(a). In all panels, coloured dotted curves represent the corresponding results from the fiducial model for comparison.

factor of a few, based on observations of dust-obscured galaxies in the rest-frame FIR band (Rowan-Robinson et al. 2016; Gruppioni et al. 2020; Khusanova et al. 2021), as well as number counts of gamma-ray bursts (Kistler et al. 2009; Robertson & Ellis 2012). If these measurements are accurate, the WFB scenario remains strongly favoured even at $z < 10^2$ Second, we may overestimate CSFRDs because our model does not account for active galactic nuclei (AGN). AGN feedback can drive significant outflows from massive galaxies, thereby reducing their surface gas densities and consequently the SFEs. Recent *JWST* observations have revealed that AGN activity becomes increasingly common at $z \lesssim 8$ (e.g. Kocevski et al. 2024). This suggests that AGN feedback may play an important role in reducing SFEs at later epochs. Therefore, incorporating the formation of supermassive black holes and their associated feedback into our model is an essential direction for future work.

---

²CSFRD estimates based on FIR fluxes vary significantly among different studies. Some report CSFRDs at $z > 5$ that are generally comparable to those derived from UV LFs (Wang et al. 2019; Riechers et al. 2020; van der Vlugt et al. 2022; Algera et al. 2023; Magnelli et al. 2024).

6 SUMMARY

In this paper, we have presented a new galaxy evolution model specialized for the early universe from $z = 20$ to 5. Our model self-consistently calculates the radially resolved mass evolution of gas, stars, heavy elements, and dust for galaxies with different dark-matter halo masses. In these calculations, we incorporate variations in the spatial extent of gas inflows (f_s), the mass loading factor of gas outflows (η), and the time-scale for dust growth (τ_{acc}). With reasonable parameter choices, our model successfully reproduces various observed properties of distant star-forming galaxies identified by *JWST* at $z > 5$. The main findings of this study are summarized as follows:

(i) The decreasing trend of UV half-light radii of galaxies for higher-redshifts is naturally explained by assuming that the spatial extent of gas inflows scales with the virial radius ($h_R = f_s \lambda_s r_{vir}$). The observed dispersion in galaxy sizes likely results from the diversity in the f_s values, which are inferred to vary in the range of $f_s = 0.1$–2. This variation could result from angular momentum redistribution in baryons, driven by disc instabilities and/or galaxy mergers.

(ii) Substantial outflows characterized by a mass loading factor of $\eta_0 \sim 5$ are necessary to explain the observed metallicity for

$z > 5$ galaxies, approximately a few times lower than the local scale relation. Similar to f_s, the η_0 values likely vary in the range $\eta_0 = 1$–100 to reproduce the diversity in the observed metallicities.

(iii) A moderately short time-scale for dust growth given by $\tau_{acc} = 5$ Myr $(Z/Z_\odot)^{-1}$ is favorable for the formation of dust-rich galaxies observed at $z \sim 7$. This time-scale allows rapid dust mass growth at $z < 8$, which is facilitated by galaxy chemical enrichment, while remaining consistent with the observational upper limit in dust mass for $z > 10$ galaxies, such as GN-z11, GHZ2, and GS-z14-0.

(iv) We have investigated star formation efficiencies (SFEs), defined as $f_* \equiv \mathrm{SFR}/(f_b \dot{M}_h)$, and found that the f_*–M_h relation is nearly redshift-independent. This relation peaks at $f_* \sim 0.2$ for haloes with $M_h \sim 10^{12}$ M$_\odot$, following scaling relations of $f_* \propto M_h$ for lower-mass haloes and $f_* \propto M_h^{-1}$ for higher-mass haloes. The value of f_* is primarily regulated by the global balance between gas supply and depletion within galaxies, leading to a negative correlation between f_* and η_0. Our predicted f_*–M_h relation closely matches observations at $z \sim 2$–7, suggesting a non-evolving mass loading factor of $\eta_0 \sim 5$ across a broad redshift range.

(v) The intrinsic UV luminosity function predicted by our model at $z = 12$ generally aligns with the observed one. This agreement arises from the high star formation efficiency mentioned above. However, our model galaxies are considerably dust-obscured due to high optical depths ($\tau_{1500} \gtrsim 10$), causing the dust-attenuated UV LF to fall far below the observed one. This trend is also confirmed at $z = 7$. These results highlight the need for potential mechanisms that effectively mitigate such significant dust attenuation over a wide redshift range.

(vi) To address the above point, we discussed three possible scenarios: (a) dust displacement, (b) large grain size, and (c) dust-to-star spatial segregation. The quantitative analysis suggests that all three scenarios can reconcile the UV LFs predicted by our model with the observed ones without significant changes in our model description. Thus, we emphasize the crucial importance of further exploring these dust processes in future theoretical studies to fully understand the observed properties of galaxies at $z > 5$.

(vii) We have also explored a weak feedback (WFB) model, in which SFRs are enhanced, and outflow rates are suppressed in dense environments with $\Sigma_g > 10^3$ M$_\odot$ pc^{-2}. This model predicts a peak SFE of $f_* \sim 0.6$, approximately three times higher than in the fiducial model, leading to higher intrinsic UV luminosities. However, as in the fiducial case, the WFB model fails to reproduce the observed UV LFs at $z > 5$, since reduced dust evacuation results in stronger dust attenuation. Thus, rather than simply increasing SFEs, mitigating dust attenuation is more crucial for resolving the discrepancy between our model predictions and the observed UV LFs in the early universe.

We emphasize that our model represents the statistically averaged nature of galaxy evolution. In reality, galaxies undergo discontinuous mergers, leading to intermittent star formation and mass evacuation through outflows, thereby establishing the diverse characteristics observed in high-z galaxies. Stochastic feedback events also play an essential role in triggering dust displacement and dust segregation processes. Therefore, validating our model prediction with cosmological galaxy formation models and simulations that incorporate these dust processes is a crucial task for achieving a more comprehensive understanding of galaxy evolution.

DATA AVAILABILITY

The data underlying this article will be shared on reasonable request to the corresponding author.

REFERENCES

Adams N. J. et al., 2024, ApJ, 965, 169
Algera H. S. B. et al., 2023, MNRAS, 518, 6142
Andrews B. H., Martini P., 2013, ApJ, 765, 140
Arrabal Haro P. et al., 2023a, Nature, 622, 707
Arrabal Haro P. et al., 2023b, ApJ, 951, L22
Arribas S. et al., 2024, A&A, 688, A146
Asano R. S., Takeuchi T. T., Hirashita H., Inoue A. K., 2013, Earth, Planets and Space, 65, 213
Bakx T. J. L. C. et al., 2021, MNRAS, 508, L58
Barnes J. E., Hernquist L. E., 1991, ApJ, 370, L65
Barnes J. E., Hernquist L., 1996, ApJ, 471, 115
Behroozi P. et al., 2020, MNRAS, 499, 5702
Bekki K., Tsujimoto T., Chiba M., 2009, ApJ, 692, L24
Bianchi S., Schneider R., 2007, MNRAS, 378, 973
Birnboim Y., Dekel A., 2003, MNRAS, 345, 349
Bournaud F., Elmegreen B. G., Elmegreen D. M., 2007, ApJ, 670, 237
Bouwens R. J. et al., 2023, MNRAS, 523, 1036
Bullock J. S., Kolatt T. S., Sigad Y., Somerville R. S., Kravtsov A. V., Klypin A. A., Primack J. R., Dekel A., 2001, MNRAS, 321, 559
Bunker A. J. et al., 2023, A&A, 677, A88
Burgarella D. et al., 2025, A&A, 699, A336
Byrne L., Faucher-Giguère C.-A., Stern J., Anglés-Alcázar D., Wellons S., Gurvich A. B., Hopkins P. F., 2023, MNRAS, 520, 722
Carniani S. et al., 2024a, A&A, 696, 14
Carniani S. et al., 2024b, Nature, 633, 318
Castellano M. et al., 2024, ApJ, 972, 143
Castellano M. et al., 2025, preprint (arXiv:2504.05893)
Chon S., Hosokawa T., Omukai K., Schneider R., 2024, MNRAS, 530, 2453
Christensen C. R., Davé R., Governato F., Pontzen A., Brooks A., Munshi F., Quinn T., Wadsley J., 2016, ApJ, 824, 57
Christensen C. R., Davé R., Brooks A., Quinn T., Shen S., 2018, ApJ, 867, 142
Correa C. A., Schaye J., Wyithe J. S. B., Duffy A. R., Theuns T., Crain R. A., Bower R. G., 2018, MNRAS, 473, 538
Cueto E. R., Hutter A., Dayal P., Gottlöber S., Heintz K. E., Mason C., Trebitsch M., Yepes G., 2024, A&A, 686, A138
Cullen F. et al., 2024, MNRAS, 531, 997
Curti M. et al., 2024, A&A, 684, A75
da Cunha E. et al., 2013, ApJ, 766, 13
D'Eugenio F. et al., 2024, A&A, 689, A152
Dayal P., Hirashita H., Ferrara A., 2010, MNRAS, 403, 620
Dayal P. et al., 2022, MNRAS, 512, 989
Dekel A., Birnboim Y., 2006, MNRAS, 368, 2
de Graaff A. et al., 2024, A&A, 684, A87
Dekel A., Sarkar K. C., Birnboim Y., Mandelker N., Li Z., 2023, MNRAS, 523, 3201
Donnan C. T. et al., 2023, MNRAS, 518, 6011

Donnan C. T. et al., 2024, MNRAS, 533, 3222

Donnan C. T., Dunlop J. S., McLure R. J., McLeod D. J., Cullen F., 2025, MNRAS, 539, 2409

Elmegreen D. M., Elmegreen B. G., Rubin D. S., Schaffer M. A., 2005, ApJ, 631, 85

Fakhouri O., Ma C.-P., Boylan-Kolchin M., 2010, MNRAS, 406, 2267

Ferrara A., 2024a, A&A, 684, A207

Ferrara A., 2024b, A&A, 689, A310

Ferrara A. et al., 2022, MNRAS, 512, 58

Ferrara A., Pallottini A., Dayal P., 2023, MNRAS, 522, 3986

Ferrara A., Carniani S., di Mascia F., Bouwens R., Oesch P., Schouws S., 2024, A&A, 694, 7

Finkelstein S. L. et al., 2015, ApJ, 810, 71

Finkelstein S. L. et al., 2023, ApJ, 946, L13

Fiore F., Ferrara A., Bischetti M., Feruglio C., Travascio A., 2023, ApJ, 943, L27

Freeman K. C., 1970, ApJ, 160, 811

Fudamoto Y. et al., 2024, MNRAS, 530, 340

Fukushima H., Yajima H., 2021, MNRAS, 506, 5512

Fukushima H., Yajima H., Omukai K., 2018, MNRAS, 477, 1071

Gibson B. K., Pilkington K., Brook C. B., Stinson G. S., Bailin J., 2013, A&A, 554, A47

Goodman J., 2003, MNRAS, 339, 937

Goulding A. D. et al., 2023, ApJ, 955, L24

Grudić M. Y., Hopkins P. F., Faucher-Giguère C.-A., Quataert E., Murray N., Kereš D., 2018, MNRAS, 475, 3511

Grudić M. Y., Boylan-Kolchin M., Faucher-Giguère C.-A., Hopkins P. F., 2020, MNRAS, 496, L127

Gruppioni C. et al., 2020, A&A, 643, A8

Hainline K. N. et al., 2024, ApJ, 976, 27

Harada N., Yajima H., Abe M., 2023, MNRAS, 525, 5868

Harikane Y. et al., 2018, PASJ, 70, S11

Harikane Y. et al., 2022, ApJS, 259, 20

Harikane Y. et al., 2023, ApJS, 265, 5

Harikane Y., Nakajima K., Ouchi M., Umeda H., Isobe Y., Ono Y., Xu Y., Zhang Y., 2024, ApJ, 960, 56

Harikane Y. et al., 2025, ApJ, 980, 138

Hashimoto T. et al., 2019, PASJ, 71, 71

Hernquist L., 1989, Nature, 340, 687

Hirashita H., Aoyama S., 2019, MNRAS, 482, 2555

Hirashita H., Ferrara A., Dayal P., Ouchi M., 2014, MNRAS, 443, 1704

Hopkins P. F., Quataert E., 2010, MNRAS, 407, 1529

Hu C.-Y., 2019, MNRAS, 483, 3363

Hutter A., Cueto E. R., Dayal P., Gottlöber S., Trebitsch M., Yepes G., 2024, A&A, 694, 15

Immeli A., Samland M., Gerhard O., Westera P., 2004, A&A, 413, 547

Inayoshi K., Harikane Y., Inoue A. K., Li W., Ho L. C., 2022, ApJ, 938, L10

Kennicutt R. C. J., 1998, ApJ, 498, 541

Kereš D., Katz N., Weinberg D. H., Davé R., 2005, MNRAS, 363, 2

Khusanova Y. et al., 2021, A&A, 649, A152

Kim J.-G., Kim W.-T., Ostriker E. C., 2018, ApJ, 859, 68

Kistler M. D., Yüksel H., Beacom J. F., Hopkins A. M., Wyithe J. S. B., 2009, ApJ, 705, L104

Kocevski D. D. et al., 2024, ApJ, 986, 30

Kohandel M., Pallottini A., Ferrara A., Zanella A., Rizzo F., Carniani S., 2024, A&A, 685, A72

Leśniewska A., Michałowski M. J., 2019, A&A, 624, L13

Li Z. et al., 2023, preprint (arXiv:2310.09327)

Li Z., Inayoshi K., Chen K., Ichikawa K., Ho L. C., 2024a, ApJ, 980, 11

Li Z., Dekel A., Sarkar K. C., Aung H., Giavalisco M., Mandelker N., Tacchella S., 2024b, A&A, 690, A108

Lisenfeld U., Ferrara A., 1998, ApJ, 496, 145

MacArthur L. A., Courteau S., Holtzman J. A., 2003, ApJ, 582, 689

Madau P., Dickinson M., 2014, ARA&A, 52, 415

Magnelli B. et al., 2024, A&A, 688, A55

Maiolino R. et al., 2024, Nature, 627, 59

Mannucci F., Cresci G., Maiolino R., Marconi A., Gnerucci A., 2010, MNRAS, 408, 2115

Maoz D., Sharon K., Gal-Yam A., 2010, ApJ, 722, 1879

Markov V., Gallerani S., Ferrara A., Pallottini A., Parlanti E., Di Mascia F., Sommovigo L., Kohandel M., 2024, Nat. Astron., 9, 458

Markov V. et al., 2025, preprint (arXiv:2504.12378)

Martorano M. et al., 2023, ApJ, 957, 46

Mason C. A., Trenti M., Treu T., 2023, MNRAS, 521, 497

Matteucci F., Greggio L., 1986, A&A, 154, 279

Matteucci F., Recchi S., 2001, ApJ, 558, 351

McKee C. F., 1989, ApJ, 345, 782

McLeod D. J., McLure R. J., Dunlop J. S., 2016, MNRAS, 459, 3812

McLeod D. J. et al., 2024, MNRAS, 527, 5004

Mitsuhashi I. et al., 2025, preprint (arXiv:2501.19384)

Morales A. M. et al., 2024, ApJ, 964, L24

Muratov A. L., Kereš D., Faucher-Giguère C.-A., Hopkins P. F., Quataert E., Murray N., 2015, MNRAS, 454, 2691

Naidu R. P. et al., 2025, preprint (arXiv:2505.11263)

Nakajima K., Ouchi M., Isobe Y., Harikane Y., Zhang Y., Ono Y., Umeda H., Oguri M., 2023, ApJS, 269, 33

Narayanan D., Conroy C., Davé R., Johnson B. D., Popping G., 2018, ApJ, 869, 70

Navarro J. F., Frenk C. S., White S. D. M., 1997, ApJ, 490, 493

Nelson E. et al., 2024, ApJ, 976, L27

Noguchi M., 1999, ApJ, 514, 77

Nomoto K., Kobayashi C., Tominaga N., 2013, ARA&A, 51, 457

Nozawa T., Kozasa T., Habe A., 2006, ApJ, 648, 435

Nozawa T., Kozasa T., Habe A., Dwek E., Umeda H., Tominaga N., Maeda K., Nomoto K., 2007, ApJ, 666, 955

Ocvirk P., Pichon C., Teyssier R., 2008, MNRAS, 390, 1326

Oesch P. A. et al., 2014, ApJ, 786, 108

Oku Y., Nagamine K., 2024, ApJ, 975, 183

Ono Y., Ouchi M., Harikane Y., Yajima H., Nakajima K., Fujimoto S., Nakane M., Xu Y., 2025, preprint (arXiv:2502.08885)

Pallottini A. et al., 2019, MNRAS, 487, 1689

Pandya V. et al., 2021, MNRAS, 508, 2979

Parlanti E., Carniani S., Pallottini A., Cignoni M., Cresci G., Kohandel M., Mannucci F., Marconi A., 2023, A&A, 673, A153

Pérez-González P. G. et al., 2023, ApJ, 951, L1

Pérez-González P. G. et al., 2025, preprint (arXiv:2503.15594)

Pizzati E., Ferrara A., Pallottini A., Gallerani S., Vallini L., Decataldo D., Fujimoto S., 2020, MNRAS, 495, 160

Pizzati E., Ferrara A., Pallottini A., Sommovigo L., Kohandel M., Carniani S., 2023, MNRAS, 519, 4608

Planck Collaboration VI, 2020, A&A, 641, A6

Reuter C. et al., 2020, ApJ, 902, 78

Riechers D. A. et al., 2020, ApJ, 895, 81

Robertson B. E., Ellis R. S., 2012, ApJ, 744, 95

Rowan-Robinson M. et al., 2016, MNRAS, 461, 1100

Rowland L. E. et al., 2024, MNRAS, 535, 2068

Sarkar A. et al., 2024, ApJ, 978, 18

Schaller G., Schaerer D., Meynet G., Maeder A., 1992, A&AS, 96, 269

Schmidt M., 1959, ApJ, 129, 243

Schouws S. et al., 2024, ApJ, 988, 8

Sheth R. K., Tormen G., 2002, MNRAS, 329, 61

Shibuya T., Ouchi M., Harikane Y., 2015, ApJS, 219, 15

Slavin J. D., Dwek E., Mac Low M.-M., Hill A. S., 2020, ApJ, 902, 135

Sommovigo L. et al., 2022, MNRAS, 513, 3122

Speagle J. S., Steinhardt C. L., Capak P. L., Silverman J. D., 2014, ApJS, 214, 15

Sugimura K., Ricotti M., Park J., Garcia F. A. B., Yajima H., 2024, ApJ, 970, 14

Todini P., Ferrara A., 2001, MNRAS, 325, 726

Topping M. W., Stark D. P., Endsley R., Plat A., Whitler L., Chen Z., Charlot S., 2022, ApJ, 941, 153

Topping M. W. et al., 2024, MNRAS, 529, 4087

Trinca A., Schneider R., Valiante R., Graziani L., Ferrotti A., Omukai K., Chon S., 2024, MNRAS, 529, 3563

Vallini L. et al., 2024, MNRAS, 527, 10

van de Voort F., Schaye J., Booth C. M., Haas M. R., Dalla Vecchia C., 2011, MNRAS, 414, 2458

van der Vlugt D., Hodge J. A., Algera H. S. B., Smail I., Leslie S. K., Radcliffe J. F., Riechers D. A., Röttgering H., 2022, ApJ, 941, 10

Venturi G. et al., 2024, A&A, 691, A19

Vijayan A. P., Thomas P. A., Lovell C. C., Wilkins S. M., Greve T. R., Irodotou D., Roper W. J., Seeyave L. T. C., 2024, MNRAS, 527, 7337

Wang T. et al., 2019, Nature, 572, 211

Wang Y.-Y., Lei L., Yuan G.-W., Fan Y.-Z., 2023a, ApJ, 954, L48

Wang B. et al., 2023b, ApJ, 957, L34

Waterval S., Cannarozzo C., Macciò A. V., 2025, MNRAS, 537, 2726

Weingartner J. C., Draine B. T., 2001, ApJ, 548, 296

Wilkins S. M. et al., 2023, MNRAS, 519, 3118

Witstok J. et al., 2024, Nature, 639, 897

Xu Y. et al., 2024, ApJ, 976, 142

Yanagisawa H. et al., 2024, ApJ, 988, 9

Yung L. Y. A., Somerville R. S., Finkelstein S. L., Popping G., Davé R., 2019, MNRAS, 483, 2983

Yung L. Y. A., Somerville R. S., Iyer K. G., 2025, preprint (arXiv:2504.18618)

Zavala J. A. et al., 2024, ApJ, 977, 9

Ziparo F., Ferrara A., Sommovigo L., Kohandel M., 2023, MNRAS, 520, 2445

APPENDIX A: $z \gtrsim 10$ GALAXIES IDENTIFIED BY *JWST*

In Table A1, we present a list of galaxies that have been spectroscopically confirmed by *JWST* at $z \gtrsim 10$. We compare the observed properties of these galaxies with our model predictions in Figs 3, 4, and 10.

APPENDIX B: POTENTIAL EFFECT OF RADIAL GAS ADVECTION

Since our model does not explicitly take into account radial gas advection, we quantitatively assess its potential effect using the results from our model. Specifically, we aim to evaluate the advection time-scale, defined as
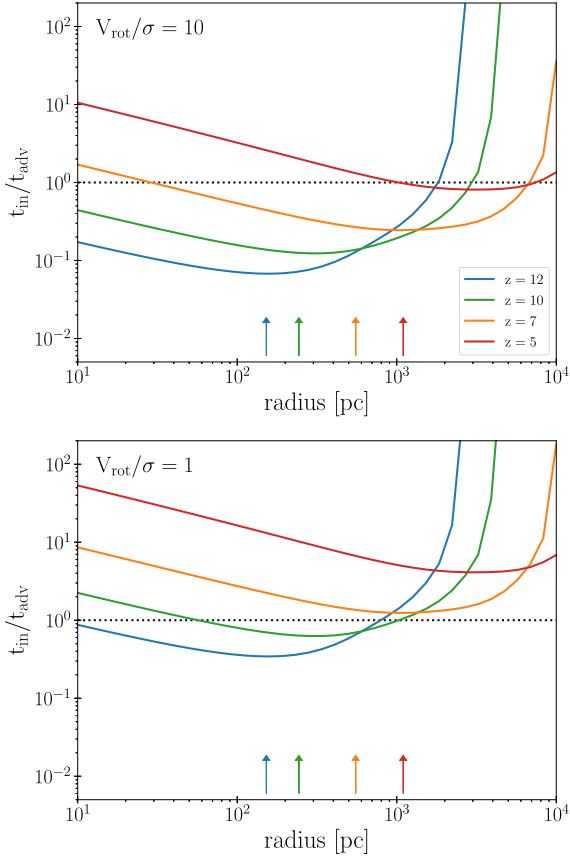
$$t_{adv} \equiv \frac{R}{v_R} . \tag{B1}$$

We assume the radial gas velocity to be $v_R = \mathcal{M} v_t$, where $\mathcal{M}$ is the Mach number and v_t is the turbulent velocity within the disc. Assuming isotropic turbulence allows us to describe the turbulent velocity as $v_t = \sqrt{3}\sigma_{los}$, where σ_{los} is the line-of-sight velocity dispersion. σ_{los} is related to the circular velocity, V_c, and the rotational velocity of the gas disc, V_{rot}, through the relation $V_c^2 \sim V_{rot}^2 + 3\sigma_{los}^2$. Under these assumptions, the advection time-scale can be rewritten as,

$$t_{adv} \sim \frac{R}{\sqrt{3}\mathcal{M} V_c} \sqrt{3 + (V_{rot}/\sigma_{los})^2} . \tag{B2}$$

To evaluate equation (B2), we adopt $\mathcal{M} = 0.1$, which generally corresponds to the theoretical upper-limit for discs where angular momentum transport is driven by non-axisymmetric spiral structures (Goodman 2003). We compute the circular velocity V_c for our model galaxies by evaluating the enclosed mass of gas, stars, and dark matter. Then, for the dark matter component, we adopt a Navarro–Frenk–White profile (Navarro, Frenk & White 1997) and model the halo concentration parameters with the fitting formula presented by (Bullock et al. 2001). As for the ratio of V_{rot}/σ_{los}, recent ALMA

Table A1. Observational data for star-forming galaxies at $z \gtrsim 10$. 1. Naidu et al. (2025), 2. Carniani et al. (2024a), 3. Carniani et al. (2024b), 4. Hainline et al. (2024), 5. Wang et al. (2023b), 6. Witstok et al. (2024), 7. D'Eugenio et al. (2024), 8. Castellano et al. (2024), 9. Mitsuhashi et al. (2025), 10. Arrabal Haro et al. (2023a), 11. Harikane et al. (2024), 12. Bunker et al. (2023), 13. Goulding et al. (2023), 14. Arrabal Haro et al. (2023b).

Name	z	M_{UV} (mag)	$\log(M_*)$ ($M_\odot$)	SFR ($M_\odot yr^{-1}$)	$12 + \log(O/H)$	R_{eff} [pc]	Reference
MoM-z14	14.44	-20.2	$8.1^{+0.3}_{-0.2}$	$13.0^{+3.7}_{-3.5}$	$7.28^{+0.65}_{-0.56}$	74^{+15}_{-12}	1
GS-z14$-$0	14.32	-20.81	$8.6^{+0.7}_{-0.2}$	19 ± 6	7.94 ± 0.03	260 ± 20	2,3
GS-z14$-$1	13.9	-19.0	$8.0^{+0.4}_{-0.3}$	$2^{+0.7}_{-0.4}$	$-$	< 160	2
GS-z13	13.2	-18.92	$7.7^{+0.4}_{-0.2}$	$1.4^{+0.6}_{-0.2}$	$-$	59	4
UNCOVER-z13	13.08	-19.4	$8.13^{+0.11}_{-0.15}$	$1.28^{+0.27}_{-0.18}$	$-$	309^{+110}_{-74}	5
GS-z13-1-LA	13.05	-18.7	$7.74^{+0.15}_{-0.12}$	$0.16^{+0.48}_{-0.15}$	$-$	62^{+11}_{-6}	6
GS-z12	12.48	-18.8	7.68 ± 0.19	$1.62^{+0.28}_{-0.24}$	7.59 ± 0.25	146 ± 11	7
UNCOVER-z12	12.39	-19.2	$8.35^{+0.18}_{-0.14}$	$2.15^{+0.81}_{-0.46}$	$-$	426^{+40}_{-42}	5
GHZ2	12.34	-20.53	$8.27^{+0.23}_{-0.18}$	$8.7^{+1.4}_{-1.9}$	$7.26^{+0.27}_{-0.24}$	34 ± 9	8,9
Maisie	11.42	-20.1	8.6 ± 0.3	2 ± 1	8	280^{+80}_{-62}	10
GS-z11	11.12	-19.32	$8.3^{+0.1}_{-0.1}$	1.45 ± 0.1	$-$	119	4
CEERS2_588	11.04	-20.4	$9.0^{+0.5}_{-0.2}$	$12.7^{+9.7}_{-4.9}$	$-$	476	11
GN-z11	10.60	-21.5	8.73 ± 0.06	$18.8^{+0.81}_{-0.69}$	$7.84^{+0.06}_{-0.05}$	64 ± 20	12
UHZ-1	10.07	-19.85	$8.14^{+0.09}_{-0.11}$	$1.25^{+0.18}_{-0.12}$	$-$	592 ± 85	13
CEERS_35590	10.01	-20.1	9.1 ± 0.1	9 ± 2	$-$	420 ± 20	14
CEERS_99715	9.97	-20.5	9.5 ± 0.1	6^{+4}_{-2}	$-$	580 ± 20	14

Figure B1. The ratio of the gas inflow time-scale ($t_{\rm in}$) to the gas advection time-scale ($t_{\rm adv}$) at each radius, predicted by our fiducial model of a halo evolving to $M_{\rm h}(z = 5) = 10^{12}$ M$_\odot$. The top and bottom panels display the results for the dynamically cold and hot discs with $V_{\rm rot}/\sigma_{\rm los} = 10$ and 1, respectively. The blue, green, orange, and red curves represent $t_{\rm in}/t_{\rm adv}$ at $z = 12, 10, 7$, and 5, respectively. To indicate the spatial extent of the galactic disc, the UV half-light radius at each redshift is indicated by upward arrows in corresponding colours. Radial gas advection can influence the gas density structure in regions where $t_{\rm in}/t_{\rm adv} > 1$ and $R < R_{\rm eff}$.

observations of $z > 5$ galaxies report a wide range of values, typically $V_{\rm rot}/\sigma_{\rm los} \sim 1$–10 (Parlanti et al. 2023; Graaff et al. 2024; Rowland et al. 2024). Supposing this diversity, we consider two extreme cases: a dynamically cold disc with $V_{\rm rot}/\sigma_{\rm los} = 10$ and a dynamically hot disc with $V_{\rm rot}/\sigma_{\rm los} = 1$. In both cases, we assume that the ratio is constant across all radii and redshifts. Under these assumptions, the advection time-scale becomes shorter at smaller radii. In particular, $t_{\rm adv} \propto R/V_{\rm c} \propto R^{1/2}$ at $R < R_{\rm eff}$, where the surface mass densities are nearly constant (see the bottom panel of Fig. 2).

Additionally, we examine the importance of radial gas advection relative to cosmological gas inflows by comparing $t_{\rm adv}$ with the gas inflow time-scale, defined as

$$t_{\rm in} \equiv \frac{\Sigma_{\rm g}}{\dot\Sigma_{\rm in}} \,. \tag{B3}$$

This gas inflow time-scale becomes longer toward lower redshifts, as $\Sigma_{\rm g}$ gradually increases while $\dot\Sigma_{\rm in}$ declines with decreasing redshifts.

Fig. B1 shows the radial profile of the ratio $t_{\rm in}/t_{\rm adv}$ at several redshifts for a model galaxy hosted by a halo that evolve to $M_{\rm h} = 10^{12}$ M$_\odot$ at $z = 5$. As expected from the behaviour of $t_{\rm adv}$ and $t_{\rm in}$ described above, this ratio increases with decreasing radii at $R < R_{\rm eff}$ and with decreasing redshifts. For the dynamically cold

case, at $z = 5$, $t_{\rm in}/t_{\rm adv}$ exceeds unity across the entire disc, suggesting that radial transport of mass and angular momentum significantly influences the disc structure. In contrast, at $z \gtrsim 7$, the entire disc shows $t_{\rm in}/t_{\rm adv} \ll 1$, indicating that the cosmological gas inflows predominantly determine the mass distribution within the galaxy.

Since the dynamically hot disc provides higher radial velocities than the cold case, it exhibits $t_{\rm in}/t_{\rm adv} > 1$ throughout the disc even at $z \sim 7$. However, even in this case, radial advection becomes subdominant compared to gas inflows at $z \gtrsim 10$. Thus, for such high-redshift galaxies, neglecting radial gas advection in our model seems a reasonable simplification. Nevertheless, we note that angular momentum redistribution could be more efficient than considered here due to strong disc instabilities (Noguchi 1999; Immeli et al. 2004; Bournaud et al. 2007) and tidal torques induced by galaxy mergers (Hernquist 1989; Barnes & Hernquist 1991, 1996; Hopkins & Quataert 2010). We thus emphasize the potential importance of radial gas advection on the galaxy evolution even at $z > 10$ and highlight this as a key topic for future investigation.

APPENDIX C: DUST OPTICAL DEPTHS IN OUR MODEL GALAXIES

We asses the effect of dust extinction in our model galaxies by evaluating the luminosity-weighted optical depth of each galaxy, defined as,

$$\overline\tau_{1500} = \frac{4\pi \int_{R_{\rm min}}^{R_{\rm max}} \tau_{1500} f_{\rm esc} I_{\rm UV} R {\rm d}R}{L_{\rm UV}} \,. \tag{C1}$$

Fig. C1 shows $\overline\tau_{1500}$ obtained by our model calculations. At $z = 12$, our model galaxies with $M_{\rm UV} \lesssim -20$ mag exhibit large optical depths of $\overline\tau_{1500} \gtrsim 10$. These high values of $\overline\tau_{1500}$ result from high surface gas densities, $\Sigma_{\rm g} \gtrsim 10^4$ M$_\odot$ pc^{-2}, combined with dust-to-gas mass ratios of $D/D_{\rm MW} \sim 0.01$, as inferred from equation (21). The emergence of heavily obscured galaxies at $z \gtrsim 10$ has been predicted by several theoretical studies (e.g. Ferrara et al. 2023, 2024; Ziparo et al. 2023). However, galaxies observed at these high redshifts tend to be extremely blue, suggesting negligible dust attenuation. This tension between theory and observation highlights the necessity of mechanisms that reduce the effective impact of dust extinction, as discussed in Sections 5.1 and 5.2.
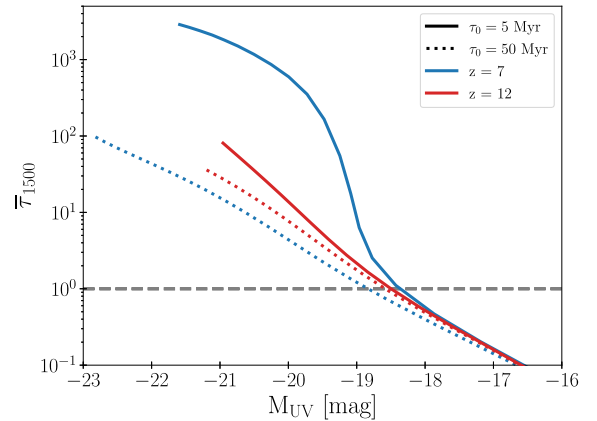
Figure C1. The luminosity-weighted dust optical depths, $\overline\tau_{1500}$, of our model galaxies as a function of dust-attenuated UV magnitude. The red and blue curves represent results at $z = 12$ and 7, respectively. The solid curves correspond to our fiducial model with a metal accretion time-scale of $\tau_0 = 5$ Myr, while dashed curves indicate results for the model with $\tau_0 = 50$ Myr.

We also note that, at $z = 12$, the optical depths and UV brightness of our model galaxies are largely insensitive to the metal accretion time-scale as far as $\tau_0 \geq 5$ Myr. In contrast, at $z = 7$, the degree of dust attenuation is highly sensitive to the choice of τ_0. In the fiducial case with $\tau_0 = 5$ Myr, $\bar{\tau}_{1500}$ increases sharply around $M_{\rm UV} \sim -19$ mag and reaches values as high as $\sim 10^3$ for galaxies with $M_{\rm UV} \lesssim -20$ mag. This sharp rise is responsible for the steep cutoff seen in our predicted dust-attenuated UV LF (Fig. 8b) and is a direct consequence of the short metal accretion time-scale, which is required to reproduce the dust content observed in $z \sim 7$ galaxies (Fig. 5b).

On the other hand, the slower metal accretion model with $\tau_0 = 50$ Myr yields optical depths at $M_{\rm UV} \lesssim -20$ mag approximately twenty times lower than those in the fiducial model. Furthermore, this model yields optical depths at $z = 7$ smaller than those at $z = 12$ by about a factor of 2. This redshift evolution reflects the combined dependencies of dust mass and galaxy size since $\bar{\tau}_{1500} \sim M_{\rm d}/R_{\rm eff}^2$.

We find that, for a fixed $M_{\rm UV}$, the dust mass does not significantly change across redshifts, although the effective radius increases toward lower redshifts, roughly following $R_{\rm eff} \propto (1 + z)^{-1}$, as shown in Fig. 3. Consequently, the optical depth approximately follows $\bar{\tau}_{1500} \propto (1 + z)^2$, thereby decreasing by ~ 40 per cent from z $= 12$ to 7. This behavior clearly does not hold in the fiducial case with $\tau_0 \geq 5$ Myr, where the metal accretion is so efficient that the dust mass increases substantially across this redshift range.

It is important to note that even with $\tau_0 = 50$ Myr, the predicted optical depths remain high ($\bar{\tau}_{1500} \gtrsim 10$) for galaxies with $M_{\rm UV} \lesssim -21$ mag, leading to an underestimation of their number densities compared to observations. Therefore, the observed UV LFs for $z > 5$ galaxies require mechanisms that reduce the optical depth, regardless of the assumed metal accretion time-scale.

This paper has been typeset from a T$_{\rm E}$X/L^{A}T$_{\rm E}$X file prepared by the author.